TESS duotransit candidates from the Southern Ecliptic Hemisphere

Faith Hawthorn [1,2]★ Sam Gill [1,2] Daniel Bayliss [1,2] Hugh P. Osborn [3] Ingrid Pelisoli [1]
Toby Rodel [1,2,4] Kaylen Smith Darnbrook,[1] Peter J. Wheatley [1,2] David R. Anderson [1,2]
Ioannis Apergis [1,2] Matthew P. Battley [5] Matthew R. Burleigh [6] Sarah L. Casewell [6]
Philipp Eigmüller [7] Maximilian N. Günther [8] James S. Jenkins [9,10] Monika Lendl [5]
Maximiliano Moyano [11] Ares Osborn [1,2] Gavin Ramsay [12] Solène Ulmer-Moll [3] Jose I. Vines [11]
and Richard West [1,2]

[1]*Department of Physics, University of Warwick, Gibbet Hill Road, Coventry CV4 7AL, UK*
[2]*Centre for Exoplanets and Habitability, University of Warwick, Gibbet Hill Road, Coventry CV4 7AL, UK*
[3]*Physikalisches Institut, University of Bern, Gesellsschaftstrasse 6, CH-3012 Bern, Switzerland*
[4]*Astrophysics Research Centre, School of Mathematics and Physics, Queen's University Belfast, Belfast BT7 1NN, UK*
[5]*Observatoire de Genève, Université de Genève, 51 Chemin Pegasi, CH-1290 Versoix, Switzerland*
[6]*Centre for Exoplanet Research, School of Physics and Astronomy, University of Leicester, University Road, Leicester LE7 7RH, UK*
[7]*Institute of Planetary Research, German Aerospace Center, Rutherfordstrasse 2, D-12489 Berlin, Germany*
[8]*European Space Agency (ESA), European Space Research and Technology Centre (ESTEC), Keplerlaan 1, NL-2201 AZ Noordwijk, the Netherlands*
[9]*Instituto de Estudios Astrofísicos, Facultad de Ingeniería y Ciencias, Universidad Diego Portales, Av. Ejército 441, Santiago, Chile*
[10]*Centro de Astrofísica y Tecnologías Afines (CATA), Casilla 36-D, Santiago, Chile*
[11]*Instituto de Astronomía, Universidad Católica del Norte, Angamos 0610, Antofagasta 1270709, Chile*
[12]*Armagh Observatory and Planetarium, College Hill, Armagh BT61 9DG, UK*

ABSTRACT

Discovering transiting exoplanets with long orbital periods allows us to study warm and cool planetary systems with temperatures similar to the planets in our own Solar system. The *Transiting Exoplanet Survey Satellite* (*TESS*) mission has photometrically surveyed the entire Southern Ecliptic Hemisphere in Cycle 1 (2018 August–2019 July), Cycle 3 (2020 July–2021 June), and Cycle 5 (2022 September–2023 September). We use the observations from Cycle 1 and Cycle 3 to search for exoplanet systems that show a single transit event in each year, which we call *duotransits*. The periods of these planet candidates are typically in excess of 20 d, with the lower limit determined by the duration of individual *TESS* observations. We find 85 duotransit candidates, which span a range of host star brightnesses: $8 < T_{\mathrm{mag}} < 14$, transit depths between 0.1 per cent and 1.8 per cent, and transit durations between 2 and 10 h with the upper limit determined by our normalization function. Of these candidates, 25 are already known, and 60 are new. We present these candidates along with the status of photometric and spectroscopic follow-up.

Key words: techniques: photometric – planets and satellites: detection – planets and satellites: general.

1 INTRODUCTION

Longer period transiting exoplanets allow us to measure the densities of warm and cool planets, assisting with studies of atmospheric composition from transit spectroscopy (e.g. Albrecht et al. 2012; Wang et al. 2021). Planetary obliquity is an indicator of planetary migration mechanisms (e.g. Albrecht et al. 2012), and long-period planets are amenable to studies of the Rossiter–McLaughlin effect (e.g. Ulmer-Moll et al. 2023) to enable determination of the spin-orbit alignment of the system. When compared to short-period hot Jupiter planets, the few well-studied long-period planets discovered to date appear to be more aligned (Rice et al. 2022), indicating possible migration mechanisms operating within the protoplanetary disc (e.g.

Madhusudhan et al. 2017). Since the launch of *Transiting Exoplanet Survey Satellite* (*TESS*; Ricker et al. 2015), a total of 392[1] exoplanets have been confirmed using *TESS* data (NASA Exoplanet Archive; Akeson et al. 2013). Of these systems, only 56 have orbital periods longer than the typical *TESS* Sector time span of 27 d.

The *Kepler* mission (Borucki et al. 2010) monitored a single 105 square degree field for approximately 4 yr, and was therefore able to discover long-period transiting exoplanets. However, most of the host stars are fainter than the capabilities of modern spectrographs to measure planetary masses and the planets cannot be confirmed and fully characterized. Hsu et al. (2019) placed a limit on the occurrence rate of $\lesssim 0.247$ planets per FGK star on orbital periods from 237–500 d. The *Kepler* exoplanet sample includes 42 planets

---

★ E-mail: faith.hawthorn@warwick.ac.uk

[1]https://exoplanetarchive.ipac.caltech.edu (2023 October 9).

with determined periods longer than 20 d with a robust mass determination from radial velocity (RV) confirmation.

The *TESS* spacecraft has completed surveys of the Southern Ecliptic Hemisphere on two occasions – in Cycle 1 (2018 July to 2019 July) and in Cycle 3 (2020 July to 2021 July). *TESS* has also re-observed the Southern Ecliptic Hemisphere in Cycle 5 (2022 September to 2023 September), but many of these observations were unavailable at the time of writing and thus are not included in this work. During these surveys a number of stars have shown a single transit (a *monotransit*), whereby one transit-like feature is found in the light curve but is not seen to repeat. With only one transit we are not able to determine the orbital period of the planet, although with prior knowledge of the star we can calculate the probability distribution for the orbital period, e.g. Osborn et al. (2022). A small number of these TESS monotransit candidates have been confirmed, e.g. Gill et al. (2020a, c) and Lendl et al. (2020).

In addition to the *TESS* monotransit candidates, there exist candidates that transit exactly once in Cycle 1 and once in Cycle 3. These candidates are *biennial duotransits*, as opposed to candidates that may have two transits in a single *TESS* cycle. For the remainder of this paper we use the term *duotransit* to refer only to such biennial duotransits. These duotransits confer two main advantages over monotransit candidates. First, the true period of a duotransit candidate is limited to a discrete set of possible periods, P_n, given by

$$P_n \in \left(\frac{\Delta T}{n} \right), n = 1, ..., n_{\max}, \qquad (1)$$

where ΔT is the time difference between the Cycle 1 and the Cycle 3 transit event and n is a whole number ranging from $n = 1$ for the longest possible period to $n_{\max}$ for the shortest possible period. Since the duration of a *TESS* sector is $\approx$27 d, we find $P_{n_{max}}$ is typically in the region of 20 d unless there is more than one Sector of data in the *TESS* Cycle 1 or Cycle 3 observations. The limited set of possible periods means it is possible to check specific orbital periods via photometric monitoring of the duotransit candidate at specific times. This is much more efficient than the continuous monitoring required to find the periods of monotransit candidates.

Secondly, duotransits are more robust against false positive signals. We can check that the two transit signals for a duotransit candidate match in depth, total duration, ingress and egress duration, limb-darkening parameters, and impact parameter. By contrast, we are far less certain that a single monotransit event is not caused by some systematic or non-planetary astrophysical event.

Cooke et al. (2018) predicted that hundreds of long-period planets would be detectable as monotransit events in the *TESS* sample, with similar results found by Villanueva, Dragomir & Gaudi (2019). Furthermore, Cooke et al. (2021) found that many of these will have a second detectable transit in Cycle 3 of *TESS* data, making the true orbital period one of an average of 38 period aliases.

Both mono- and duotransits require extensive follow-up with both photometric and RV observations in order to confirm the transit signal, orbital period, radius, and mass. Constraining the period of a candidate can greatly reduce the number of RV measurements needed to confirm the exoplanet and measure its mass (e.g. Gill et al. 2020c).

In this paper we set out our search for duotransits from the Cycle 1 and Cycle 3 *TESS* Full-Frame Image (FFI) light curves. In Section 2 we describe the *TESS* data that we use to search for duotransit candidates. In Section 3 we outline our search algorithm and vetting procedure. In Section 4 we set out the results of our search, including the details of the 85 duotransit candidates. Finally in Section 5 we

discuss the prospects for confirming these duotransit candidates via follow-up photometric and spectroscopic programmes.

2 TESS OBSERVATIONS

TESS is a space-based NASA mission focusing on the discovery of transiting exoplanets around bright stars (Ricker et al. 2015). *TESS* has four cameras, each equipped with a grid of four CCDs for a total combined field of view of TESS of $24° \times 96°$. In Cycle 1 (2018 July 25–2019 July 17), *TESS* observed almost the entire Southern Ecliptic Hemisphere in 13 sectors, each observed for a period of approximately 27 d. Each *TESS* sector has a gap of approximately 2.4 d, during which time the satellite downlinks data. There is a similar gap in between sectors. Other gaps in the data can be due to technical problems with the spacecraft or scattered light (mostly from the Earth) making some image frames unusable (e.g. Dalba et al. 2020). Select stars were observed with 2 min cadence, while the FFIs were observed with a cadence of 30 min.

TESS reobserved the Southern Ecliptic Hemisphere in Cycle 3 (2020 July 5–2021 June 24), with the FFIs collected with a shorter cadence of 10 min. During Cycle 3, *TESS* slightly shifted its survey fields in order to cover spatial gaps in between the Cycle 1 sectors.

For our search for duotransit candidates, we use the *TESS* FFI light curves produced by the Science Processing Operations Center pipeline (SPOC; Jenkins et al. 2016), which are publicly available from the Mikulski Archive for Space Telescopes (MAST).[2] The SPOC pipeline produces FFI light curves for approximately 160 000 stars per sector, based on selection criteria set out in Caldwell et al. (2020).

We focus solely on the Southern Ecliptic Hemisphere, as at the time of writing *TESS* had completed its campaign of the Southern Ecliptic in two cycles. We use Sector 1–13 data from Cycle 1, and Sector 27–38 data from Cycle 3. In total, this results in a sample of 1422 473 stars. We search light curves from the Presearch Data Conditioning Simple Aperture Photometry (PDCSAP; Smith et al. 2012; Stumpe et al. 2012, 2014) light curves, which have instrumental systematic trends removed from the Simple Aperture Photometry (SAP) flux, but should retain stellar variability including any transit events.

In addition to using flux measurements from the FFI PDCSAP light curves, we also use the sky background and momentum centroiding measurements provided in the PDCSAP light-curve files via the keywords SAPBKG and MOMCENTR1/MOMCENTR2, respectively. These data allow us to rule out a large number of false candidates as described in Section 3.2.

3 DUOTRANSIT SEARCH

Our search for *TESS* duotransit candidates arises out of a more general search for *TESS* monotransits. We therefore begin by searching the entire set of 1422 473 SPOC PDCSAP FFI light curves for monotransit events, and then we match up events to detect duotransit candidates.

3.1 Searching for monotransit events

We begin by downloading the SAP and PDCSAP SPOC FFI light-curve products from MAST. To remove bad data points from the light curves we discarded data points with QUALITY bit values above 0. We read the meta information for each light curve, including the TIC ID,

---

[2]Accessible at https://mast.stsci.edu/.

effective temperature, stellar radius, and metallicity if available. We assume a solar metallicity of 0 dex for stars with no metallicity value available. We split each light curve into segments defined by gaps in excess of 2.4 h and normalize each separately. This accounts for gaps in individual orbits due to spacecraft data download times and regions of data flagged by the SPOC algorithm. For each segment, we smooth the light curve using an iterative Savitzky–Golay filter (five iterations using a threshold of 3σ) with a window size 48 h (e.g. Hattori et al. 2022). This window size strikes a balance of removing stellar activity but ultimately sets an upper limit on the width of transit events our algorithm can detect. Our tests show that transit widths below ~2.3 d are easily detectable using this filter width. For events wider than this, we find that the Savitzky–Golay filter begins to confuse transit signals with stellar activity and thus the event is not recovered. In addition, our tests showed that the change in cadence between Cycle 1 (30 min) and Cycle 3 (10 min) had a negligible effect on the filter. For a warm Jupiter in a circular orbit around a Solar type star, we estimate an upper limit to the possible recovered orbital periods of in excess of 1000 d.

Once the light curves are normalized and flattened, we pass them to `monofind`, our custom monotransit detection algorithm. `monofind` searches for monotransit events in the light curve where three consecutive 30-min data points are 3 median absolute deviations below the normalized median of the light curve. An example of this method is shown in Fig. 1, as applied to TOI-2447 (Gill et al., submitted). For the Cycle 1 light curves we use the native 30 min data points, while for the Cycle 3 light curves we bin the native 10-min cadence by three to a 30-min cadence to achieve a consistent detection threshold for transit events.

3.2 Selecting duotransit candidates

After searching all the *TESS* Cycle 1 and Cycle 3 SPOC FFI light curves for monotransit events, we cross-match detections to search for stars which show exactly one monotransit event in Cycle 1 and one monotransit event in Cycle 3. This yielded a list of 9718 duotransit candidates.

We then performed a visual inspection of these 9718 light curves to check which of these showed two events that could possibly be transit events. This allowed us to remove obvious false positives that had triggered the `monofind` algorithm but did not have two transit-shaped events in the light curve. In most instances these were some kind of variable star. This quick visual inspection took us down to a total of 736 reasonable duotransit candidates. The majority of candidates that did not pass this vetting step were caused by asteroids passing through the target and/or background pixel apertures, systematics noise events due to the spacecraft, or changes in the amplitude of variable stars (see examples presented in Fig. 2).

We examined each of these duotransit candidates in order to ascertain which appeared to be good transiting exoplanet candidates, and which were false-positives. Examples of false-positive scenarios included those causing transit-like events such as eclipsing binary stars, *TESS* spacecraft systematics (in particular momentum dumps), stellar variability, and Solar system asteroids passing through the background and target photometric aperture.

We are able to identify events caused by asteroids crossing the photometric aperture by checking for variations in the sky background (SAPBKG) that correlate with the monotransit event. We also noticed that such events were typically very asymmetrical in shape, and therefore unlike a bona fide monotransit event. In total, we identified 170 of our initial duotransit candidates as being due to asteroids crossing the photometric aperture in Cycle 1 or Cycle 3.
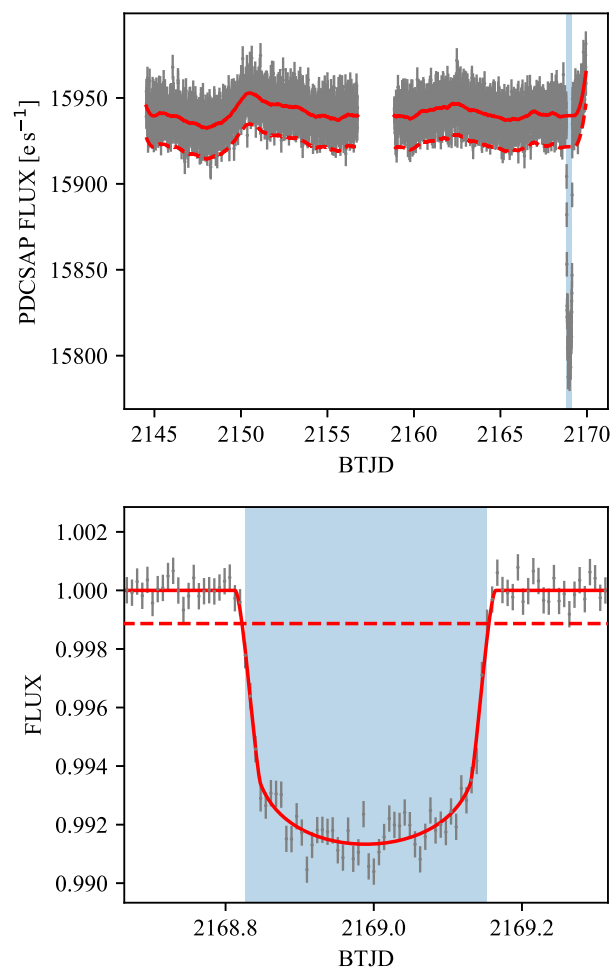
Figure 1. *Upper panel:* the *TESS* Sector 32 light curve of TOI-2447 (black) with detrending model (red solid line) and the 3-MAD detection threshold (red dashed line). A single event was detected (highlighted in blue). *Lower panel:* an inspection of the transit event with the best-fitting transit model (red solid line).

We identified monotransit events that were likely caused by eclipsing binaries by examining the results from the transit/eclipse fit from `monofind`. We designated any event with a modelled companion radius $> 2\,R_J$ ($\sim 22\,R_\oplus$) to be an eclipsing binary, and removed it from our duotransit candidate list. Such well-separated planets are not expected to be inflated like hot Jupiters (e.g. see fig. 2 from Lopez & Fortney 2016) and thus this limit is justified. We also designated a candidate as an eclipsing binary if there was evidence of a secondary eclipse in the light curve. Furthermore, we excluded events which had significant depth differences between Cycles 1 and 3. In total we identified 384 eclipsing binaries from our our initial duotransit candidate list.

We searched for blended eclipsing binaries by inspecting the light curves of nearby stars, by checking for centroiding offsets during the monotransit events, and by examining the target pixel file (TPF) using our custom `spoctpf` tool. `spoctpf` allows us to make a light curve for any pixel or set of pixel in the TPF, and helps determine if the monotransit event is on the star of interest, or is on a nearby star. In total we identified 58 blended eclipsing binaries from our our initial duotransit candidate list.

We also examined the pre-normalized and pre-flattened PDCSAP light curves, as well as the SAP light curves. This was to ensure
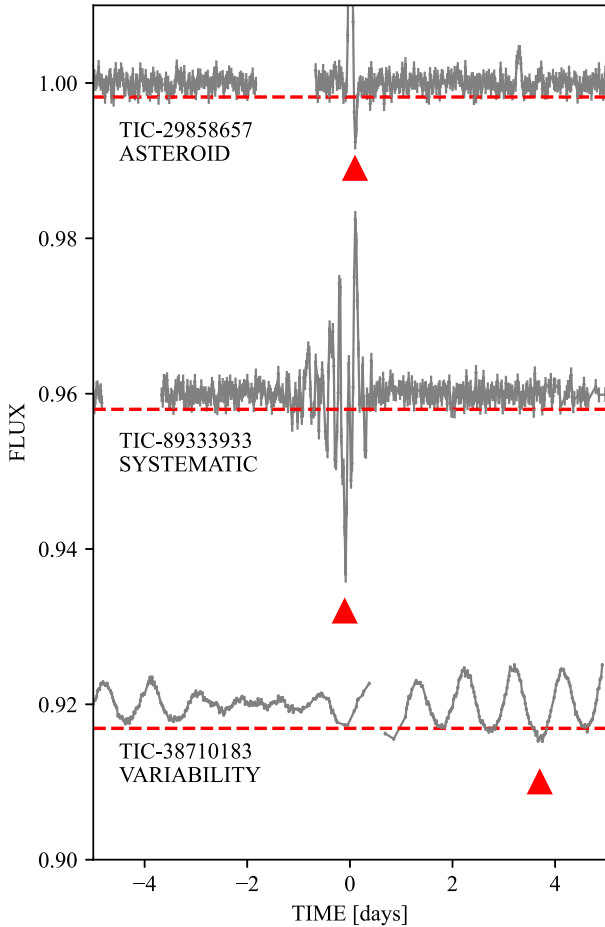
Figure 2. Three example duotransit candidates ruled out during the visual inspection of the transit events in the *TESS* light curves, with an arbitrary flux offset for clarity. The dotted red line indicates the 3 median absolute deviations detection threshold used in `monofind`. The red triangles indicate the event that triggered the detection by `monofind`. From top to bottom, these example events are caused by an asteroid passing through the target and background aperture, systematic noise caused by the spacecraft, and changes in amplitude of a variable stars.

that neither the PDCSAP algorithm nor our own normalization and flattening had significantly altered the shape of the detected monotransit events. We also inspected by-eye the full unflagged SPOC light curve for additional transit events that may have been excluded from the PDCSAP data.

Finally we checked if any of the duotransit candidates had an associated Data Validation Report (DVR, Twicken et al. 2019). DVRs are created for potential *TESS* planets candidates processed with the SPOC pipeline and contain initial findings about the system including a detailed model fit and analysis of nearby stars to exclude blend scenarios. If a DVR determined a candidate to be a false-positive, we investigated the target further to assess if it warranted exclusion from our list.

Some candidates displayed depth differences between the Cycle 1 and Cycle 3 events. SPOC light curves use unique masks for each individual Sector which may lead to different amounts of dilution from neighbouring stars depending on telescope pointing and orientation for each sector (Bryant, Bayliss & Van Eylen 2023). This should be accounted for in the detrended SPOC data (PDCSAP) but might not be perfect, and thus small sector-dependent depth
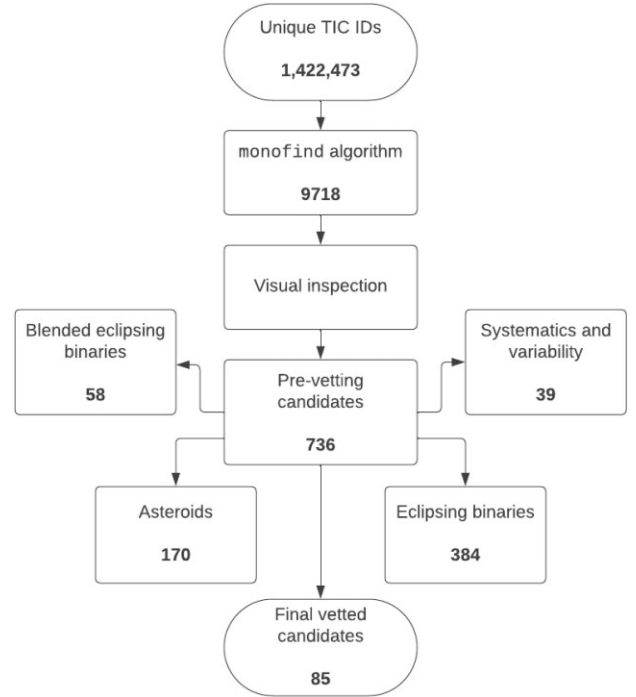
Figure 3. Flowchart of the `monofind` algorithm candidates and the vetting process that followed, with the number of candidates categorized at each stage as blended eclipsing binaries (blends), asteroids, eclipsing binaries, and other systematics and stellar variability features.

differences are expected ($\lesssim 2$ ppt), particularly in crowded fields. Some candidates had larger depth and width differences, which could be multiplanet systems or blended eclipsing binaries. However, since they do not meet our criteria for selection as duotransit candidates, they were excluded from our list. We also found 39 duotransit candidates that we associate with spacecraft systematics (stray light, momentum dumps, etc.[3]). This number also includes a few events resulting from stellar variability that was poorly matched by our detrending model.

A flowchart illustrating the candidate search and vetting process, and the associated numbers of candidates categorized at each stage, is shown in Fig. 3.

In summary, out of the 1422 473 unique TIC IDs, 9718 duotransit candidates were identified by the `monofind` algorithm, and after visual inspection this was reduced to 736 candidates pre-vetting. As a result of the vetting process, 58 objects were classified as blended eclipsing binaries (blends), 170 as Solar system asteroids, 384 as eclipsing binaries, and 39 as events caused by either spacecraft systematics or poorly detrended stellar variability. We list a sample of these events along with their designation in Table A4. The vetting process left us with a final number of 85 duotransit candidates that we present as likely planetary in nature in this paper.

3.3 Modelling candidate duotransit events

In order to derive planetary parameters for the candidates, as well as the most likely period aliases, we must fit the available transits. However, most transit model fitting requires a priori knowledge of the orbital periods, and is certainly not optimized to sample the extremely

---

[3]*TESS* Instrument Handbook; https://archive.stsci.edu/tess/tess_drn.html.

narrow but widely separated period regions found for duotransits. We used the `MonoTools` package (Osborn 2022) which fits transits in a way agnostic of orbital period and then computes the posterior density function of the planet candidate from the orbital velocity implied from the transit impact parameter, radius ratio and duration. This has previously been used to model other duotransiting planet candidates that were subsequently confirmed (e.g. Osborn et al. 2021, 2022).

`MonoTools` fits transits using the `exoplanet` python library (Foreman-Mackey et al. 2021). Stellar parameters from the *TESS* Input Catalogue (TICv8; Stassun et al. 2019) were used as priors for each of the fits; as was the Kipping (2013) eccentricity prior, the Espinoza & Jordán (2016) impact parameter prior, and quadratic limb-darkening parameters constrained using theoretical predictions for the *TESS* bandpass of Claret (2017). In the majority of cases, a cubic spline was fit to the transit-masked *TESS* PDCSAP flux in order to pre-flatten the light curve and a window of 5.5 transit durations was cut around the transit. However, after modelling some of these fits appeared to poorly model the out-of-transit variability. In these cases we turned to a simple harmonic oscillator (SHOTerm) `celerite` Gaussian process (Foreman-Mackey et al. 2017), which we constrained by first sampling out-of-transit data and then using the inferred hyperparameter distributions as priors for a combined model fit. A log scatter parameter was used to encapsulate additional noise for each transit. The transit model was then sampled using the Hamiltonian Monte Carlo of Salvatier, Wiecki & Fonnesbeck (2016) using a burn-in phase of 800 steps and 1500 samples on each of four independent chains, resulting in typical effective sample sizes of 2500–3000 for each parameter for each candidate. The derived parameters are shown in full online but summarized in Table A3. The probabilistic planetary period distributions are shown in Table A3 and in Fig. 4 ordered from shortest to longest.

4 RESULTS

4.1 85 duotransit planet candidates

Following the methods described in Section 3, we have found a total of 85 duotransit planet candidates from our `monofind` search and vetting of the SPOC FFI light curves for the Southern Ecliptic *TESS* fields (Sectors 1–13, 27–34). The stellar properties of our candidates are set out in Table A1, where N_{sec} denotes the total number of *TESS* sectors in which the target was observed. The transit event parameters are set out in Tables A2 and A3, including the central transit times T_{c1} and T_{c2} of the Cycle 1 and Cycle 3 events, respectively, and the separation between the two events in days ΔT_c. We also include the *Gaia* flags of non-single star (NSS), where 0 denotes a good single-star solution, 1 denotes an astrometric binary, 2 denotes a spectroscopic binary, and 3 denotes an eclipsing binary; and the *Gaia* robust RV amplitude in km s^{-1}, calculated using the standard deviations of individual RV measurements as set out in *Gaia* Data Release 3 (DR3, Gaia Collaboration 2022). We do not remove candidates from our target list based on these values, however, since an NSS designation is often consistent with the presence of a planet and it is not clear how robust the *Gaia* DR3 RV amplitudes are (e.g. Seabroke et al. 2021). In Table A3, we also show the most probable value of P_n (P_{marg}) and the corresponding value of n (N_{alias}).

The transit events for all 85 duotransit candidates are plotted in Figs A1–A5. We plot the best-fitting transit and eclipse model for each event from the `monofind` algorithm (see Section 3.1). We also plot the sky distribution of the candidates in Fig. 5.

Fig. 6 shows where our duotransit candidate host stars lie on the HR diagram, with most on the main-sequence spanning spectral types A–K, some on the main-sequence turn-off, and one in the hot sub-dwarf regime (see Section 4.2). Our candidates span a range of brightness: $8 < T_{mag} < 14$, with most candidates lying in the range $10 < T_{mag} < 13$; see Fig. 11. This magnitude range is largely governed by the magnitude distribution of the SPOC FFI light curves that cuts off at around $T_{mag} = 13.5$ due to the number of light curves per sector being restricted to approximately 160 000 (Jenkins et al. 2016).

We calculated the total signal-to-noise ratios (SNRs) for each of our candidates as a function of the SNRs of each individual transit event. The SNR of each transit event was estimated using the double box approximation model described by Kipping (2023). Using this square well transit model, the SNR for each transit event with a depth δ in ppm, a duration T_{dur} in hours, light curve noise σ in ppm, and a contamination ratio C was calculated using equation (2):

$$\text{SNR} = \frac{1}{C} \times \frac{\delta}{\sigma} \sqrt{T_{dur}}. \tag{2}$$

The contamination ratio and noise value were both extracted directly from the headers of the SPOC light curves. In some cases these values were missing from the headers of the Cycle 3 light curves; in such instances we used the same noise as the Cycle 1 light curve. To combine the SNR across both transit events we add the individual SNR for each event in quadrature.

We plot the distribution of the total SNR values for our 85 candidates in Fig. 7, and find that most candidates have SNR between 10 and 70, with the distribution peaking at SNR values of 25–30. There is one candidate with a total SNR value below 10 and four candidates with an SNR value above 100.

4.2 Candidates of special interest

Based on our *Gaia* H-R diagram in Fig. 6, we identify three candidates that are distinct from the rest.

4.2.1 A1V type host star, TIC-221915858

TIC-221915858 (candidate 45) is the most luminous star in our sample and resides in the region of the colour–magnitude diagram where the main-sequence approaches the sub-giant branch (Fig. 6). This is complemented by *Gaia* DR3 stellar parameters suggesting that TIC-221915858 is a hot ($T_{eff} = 9000$ K) A1 star with a renormalized unit weight error of 0.814 indicative of a good astrometric solution. The fitted spectral energy distribution (SED) in TIC V8, which uses *Gaia* DR2 along with 2MASS colours, suggests TIC-221915858 is a main sequence A1 ($T_{eff} = 9475 \pm 187$ K) star with mass and radius of 2.41 ± 0.33 M$_\odot$ and 2.47 ± 0.09 R$_\odot$, respectively. In addition to being the most luminous host star in our sample, TIC-221915858 is also the hottest on the main sequence and represents an undersampled population of exoplanets around hot stars. If a planet is confirmed around TIC-221915858, it would be the hottest planet host star discovered by the *TESS* mission.[4] The 5.74 ppt transit depth is detectable with ground-based photometric facilities and so it is possible to recover the orbital period with ground-based instruments. However, recovering the spectroscopic orbit will be challenging, in-part due to the typical rotation and lack of absorption lines in A-type stars making it difficult to measure a precise cross-correlation function (CCF) centre. Doppler tomography (e.g. Watson et al. 2019) has been used successfully to determine the radial-velocity semi-amplitude of fast-rotating stars with broad CCFs (Temple et al. 2018,

---

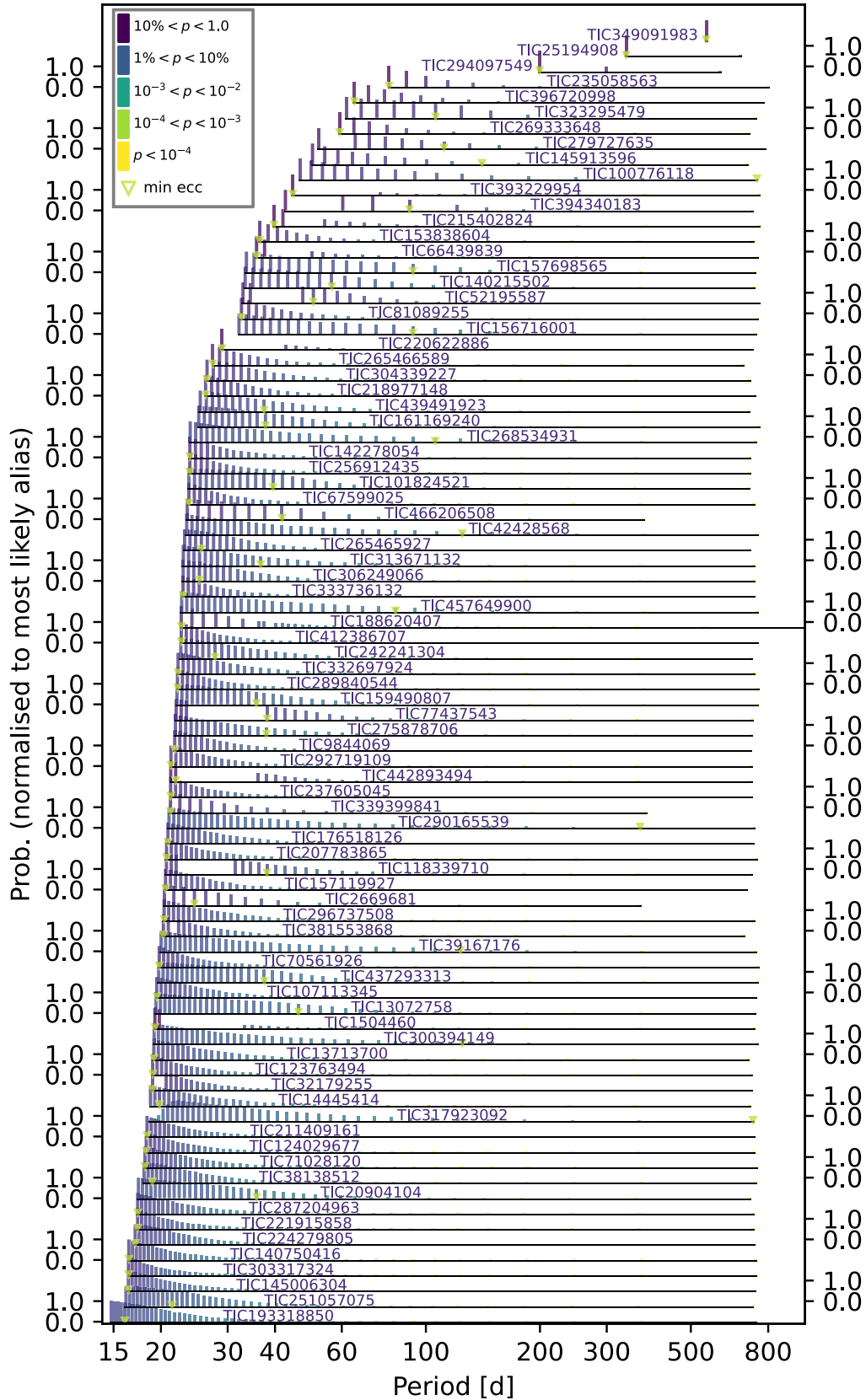[4]exoplanetarchive.ipac.caltech.edu (as of 2023 October 10).

Figure 4. Probability distribution of possible periods for each duotransit candidate as computed by `MonoTools`, normalized to the most likely period alias. The vertical colourbars refer to six steps in the log probability of each alias, and the green triangles represent the minimum eccentricity aliases.
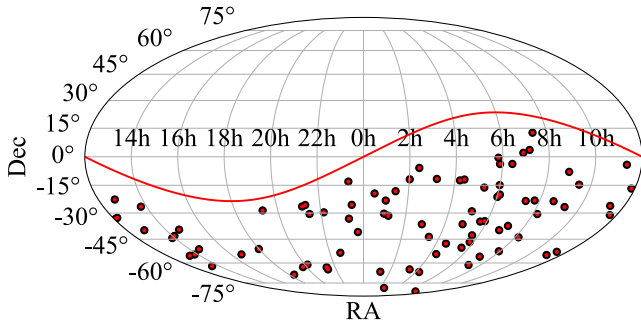
Figure 5. The ecliptic plane (solid red line) with the positions of the 85 duotransit candidates marked with red-inset black points.

2019) and could be applicable to TIC-221915858 once the orbital period is known. We provide the light curves and transit models for this candidate in Fig. A2.

4.2.2 Late K-dwarf host, TOI-4310/TIC-303317324

While the majority of our duotransit candidates orbit F, G, and early K type dwarf stars, the candidate TOI-4310 (TIC-303317324, candidate 65) is a late K-dwarf star with $T_{eff} = 4159$ K. This is an outlier amongst our candidates on the *Gaia* colour–magnitude diagram (Fig 6), positioned much further down the main sequence than any of our other candidates. The estimated radius of TOI-4130 is 0.72 R$_\odot$, and the transit model indicates the transiting planet would have a radius of 2.67 R$_\oplus$, making it one of the smallest of our duotransit planet candidates. We provide the light curves and transit models for this candidate in Appendix Fig. A1.

4.2.3 Hot subdwarf host, TOI-709/TIC-396720998

TOI-709 (TIC-396720998, candidate 78) has two ∼6 ppt deep transits with durations of ∼4.3 h. It is the only candidate in our list categorized as a hot subdwarf host star (LB 1721; Culpan et al. 2022), residing on the $G_{BP} - G_{RP} < 0$ region of the colour–magnitude diagram in Fig. 6 outside of the main population of exoplanet hosts from our candidates. Hot subdwarfs are evolved compact stars, mainly resulting from enhanced mass-loss at the tip of the red giant branch, which likely occurred due to binary interaction (Maxted et al. 2001; Han et al. 2002, 2003; Pelisoli et al. 2020). This makes them targets of interest for probing the survivability of planets to both stellar evolution and binary environments. Most hot subdwarf companions fall into two populations containing either close white dwarf or M-dwarf/brown dwarf companions or wide FGK-type companions (e.g. Schaffenroth et al. 2022), with no planetary companions confirmed to date (e.g. Van Grootel et al. 2021; Thuillier et al. 2022).

Parameters from TICv8 poorly constrain the mass and a radius of the host to 0.5 ± 0.3 M$_\odot$ and 0.15 ± 0.11 R$_\odot$ (log $g = 5.8 \pm 0.9$), which are consistent with a hot subdwarf and make it the smallest candidate host star in our list. Jeffery, Miszalski & Snowdon (2021) obtained for this star a T_{eff} of 45 600 ± 1000 K and a consistent log g of 6.08 ± 0.04 and classified it as helium-rich sdO (He-sdO). They reported no radius or mass estimate. To derive a radius consistent with the precise T_{eff} and log g of Jeffery et al. (2021), we performed an SED fit using `speedyfit`.[5] We employed spectral models

[5]https://speedyfit.readthedocs.io/.

from the Tübingen NLTE Model-Atmosphere Package (TMAP, Werner & Dreizler 1999; Rauch & Deetjen 2003; Werner et al. 2003). Initial attempts revealed the existence of excess flux towards the red/near-infrared compared to the hot subdwarf model. We therefore included a second component in the fit, modelled with ATLAS9 spectra (Castelli & Kurucz 2003). The log g was kept fixed at the spectroscopic value for the hot subdwarf (as it is poorly constrained by a SED fit), and a Gaussian prior was applied on the temperature. The temperature of the companion star was allowed to vary freely within 3500 and 6000 K (restricted by the lack of contribution to the spectrum in Jeffery et al. 2021: higher temperatures would lead to visible lines in the spectrum; for lower temperatures, the hot subdwarf would completely dominate and a companion would have no effect) and the log g was left to vary in the range of 4 to 5. A prior on the *Gaia* parallax was also applied, which enables the determination of precise radii. The MCMC fit converged to radii of $0.18^{+0.06}_{-0.03}$ R$_\odot$ and $0.88^{+0.30}_{-0.15}$ R$_\odot$ for the hot subdwarf and the companion, respectively. The companion T_{eff} was found to be 5100 ± 120 K, consistent with a K-type main sequence star. FGK-type companions are found with 30 per cent of hot subdwarfs (Stark & Wade 2003), and their periods are in the range of 100–1000 d (e.g. Vos et al. 2019), which could be consistent with the orbital period of the duotransit signal. We note that there is also another much deeper (5.8 per cent) transit/eclipse signal with a 32 d period that is reported in *TESS* Follow-up Observing Program (TFOP), and was the reason this candidate was flagged as a TOI. However that signal is distinct from the duotransit signal that we report in this paper. We provide the light curves and transit models for this candidate in Appendix Fig. A4.

4.3 Other notable candidates

4.3.1 Continuous viewing zone candidates

Three of our candidates lie inside or close to the *TESS* continuous viewing zone, where targets are observed in every Sector. TIC-25194908 (candidate 8) was observed in Sectors 1–13 during Cycle 1, and Sectors 27–38 in Cycle 3, for a total of 24 sectors, with only two transits detected. TIC-294097549 (candidate 62) was observed in multiple Sectors across Cycle 1 and Cycle 3 for a total of 13 sectors, also with only two transits detected. This additional *TESS* coverage rules out most alias periods, and only two and three periods are possible, respectively, for these candidates. These are likely to be among the longest periods from our sample, with the remaining allowed periods in the range 337–675 and 299–599 d, respectively (see Table A3).

TIC-349091983 (candidate 74) was observed in all sectors in Cycle 1 with the exception of Sector 5, and again in Cycle 3 in all sectors with the exception of Sector 35, for a total of 24 sectors. There is only one possible period for this candidate of approximately ∼549 d, and thus the true orbital period is solved from *TESS* alone.

4.3.2 TESS *Objects of Interest and Community* TESS *Objects of Interest candidates*

TESS Objects of Interest (TOIs) are planet candidates that have been vetted by the *TESS* Science Office, the TFOP and designated as promising candidates for follow-up and publication. 11 of our total 85 candidates have previously been flagged as TOI, and these are labelled in Table A1.

Another 14 of our 85 candidates have previously been flagged as Community *TESS* Objects of Interest (CTOIs), and these are also labelled in Table A1. CTOIs are typically planet candidates
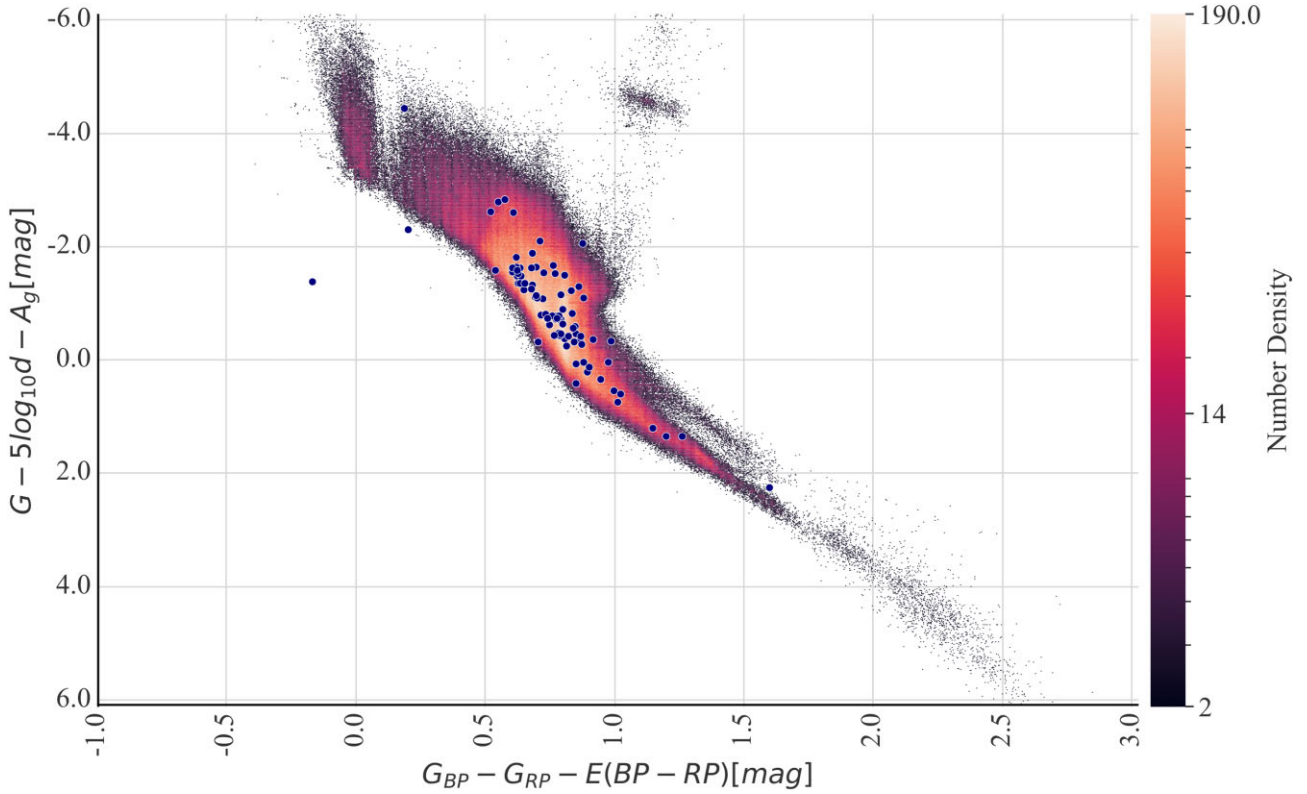
Figure 6. *Gaia* DR3 (Gaia Collaboration [2022]) colour–magnitude diagram (corrected for extinction and reddening) showing all stars with *TESS* FFI SPOC light curves from Cycle 1 and Cycle 3 that have measured *Gaia* DR3 distances. The blue circles indicate the positions of our 85 duotransit candidates. The colourbar shows the relative number density of stars at each location in the diagram. For six of the duotransit candidates there was no *Gaia* DR3 distance measurement (see Table [A1]) so we estimate the distance from the parallax and do not correct for reddening or extinction.
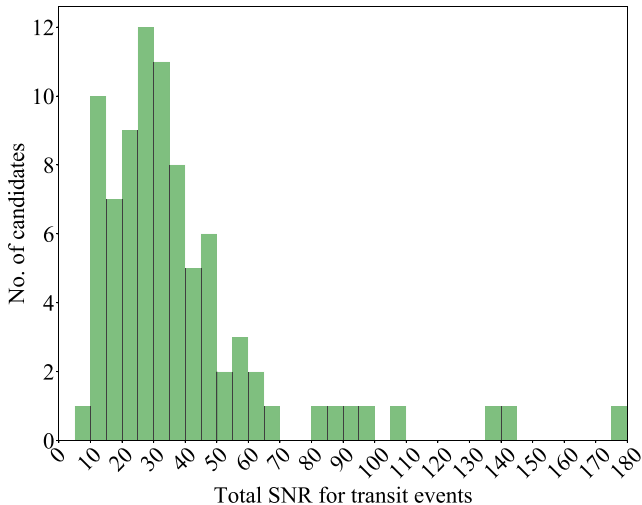
Figure 7. The distribution of total transit event SNR values (see Section [4.1]) for our 85 duotransit candidates.

submitted by additional community projects outside of the official TOI planet search pipelines, and CTOIs are reviewed by the *TESS* TOI team before being promoted to TOI status and assigned a number.

The majority of CTOIs have been identified by the *WINE* (Warm gIaNts with tEss) collaboration (e.g. Jordán et al. [2020]; Schlecker et al. [2020]; Hobson et al. [2021]), the *PHT* (Planet Hunters *TESS*)

project (Eisner et al. [2021]), and the *STF* (Single-Transit Finder) project.

4.3.3 Confirmed and published candidates

Two of our duotransit planet candidates have already been confirmed and published. TOI-5153 (candidate 25; TIC-124029677) has been published by Ulmer-Moll et al. ([2022]). The planet is a large warm Jupiter (M $= 3.26^{+0.18}_{-0.17}$ M$_J$, R $= 1.06^{+0.04}_{-0.04}$ R$_J$) orbiting an F8-type star on a period of 20.33 d. We find that our fitted planetary radius from Table [A3] is in agreement with this published value. TIC-466206508 (candidate 85; TOI-5542) has also been published by Grieves et al. ([2022]). The planet is an old warm Jupiter orbiting a relatively metal-poor G-dwarf host star on a period of 75.12 d, with a mass of M $= 1.32^{+0.10}_{-0.10}$ M$_J$ and a radius of R $= 1.01^{+0.04}_{-0.04}$ R$_J$. Other publications for these solved systems are forthcoming, e.g. TIC-77437543 (Henderson et al. 2023, in preparation), TIC-333736132 (Kendall et al. 2023, in preparation), and TIC-224279805.

4.4 Previous TOIs and CTOIs identified as false positives

Some of the candidates that were detected in our transit search but rejected as false positives have previously been announced as TOIs or CTOIs. In all cases, we found these to be examples of passing asteroids that caused peaks in the SAP background time series and hence false dips in the target light curve (see Section [3.2]). These false positives are are TOI-4312 (TIC-251086776) and the CTOIs TIC-152070435 and TIC-275180352.
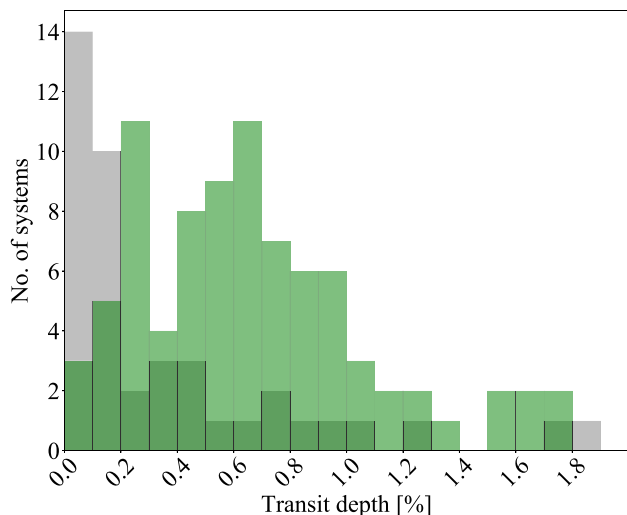
Figure 8. The distribution of transit depths for our duotransit candidates (green) and the confirmed *TESS* discovered exoplanets from the Southern Ecliptic Hemisphere (grey).

5 DISCUSSION

From our initial set of 1 422 473 unique TIC IDs, 9718 were identified as duotransit candidates from our `monofind` algorithm in the first instance, and after a quick visual inspection to reject obvious variable stars this was reduced to 736 candidates pre-vetting (see Section 3.2). From these candidates, 651 were determined to be caused by false-positive scenarios including blended sources, asteroid crossing events, eclipsing binaries, systematics, and stellar variability. This leads to a final list of 85 duotransit candidates presented in this work (see Section 4 and Tables A1–A3).

We have submitted all of our non-TOI/CTOI duotransit planet candidates to the TFOP (60 candidates). We hope that this will allow the community to follow up these interesting systems further with the aim of determining their true orbital periods and providing confirmation and full characterizations of new long-period planets.

5.1 Duotransit candidate properties

We plot the transit depths of our 85 duotransit candidates in Fig. 8, and for comparison we overlay the *TESS* planets that have been confirmed in the Southern Ecliptic Hemisphere.[6] The transit depths of our duotransit candidates range from approximately 0.1 per cent to 1.8 per cent, peaking around 0.7 per cent. This is significantly deeper than is typical for the confirmed *TESS* exoplanets, the majority of which are less than 0.2 per cent. This depth difference is to be expected given that the `monofind` algorithm is designed to detect individual high-SNR transits, which will naturally be deeper than the general TOI population.

In Fig. 9 we plot the best-fitting radii of our duotransit planet candidates, again in comparison with the *TESS* confirmed planet sample. We find that our sample peaks at around the radius of Jupiter (11 $R_\oplus$), which is also to be expected for a sample on individual high-SNR transits. Our sample extends to radii exceeding 16 $R_\oplus$, and while the sample of confirmed *TESS* planets also extends to similar radii, these are hot Jupiters with radii inflated by irradiation, which we
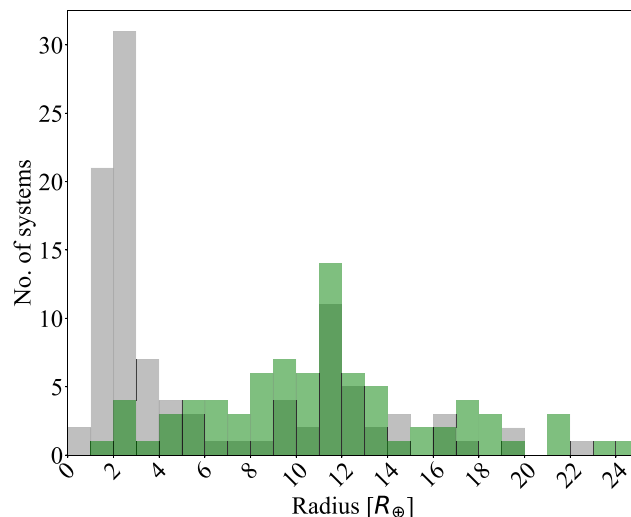
Figure 9. The distribution of planet radii for our duotransit candidates (green) and the confirmed *TESS* discovered exoplanets from the Southern Ecliptic Hemisphere (grey).
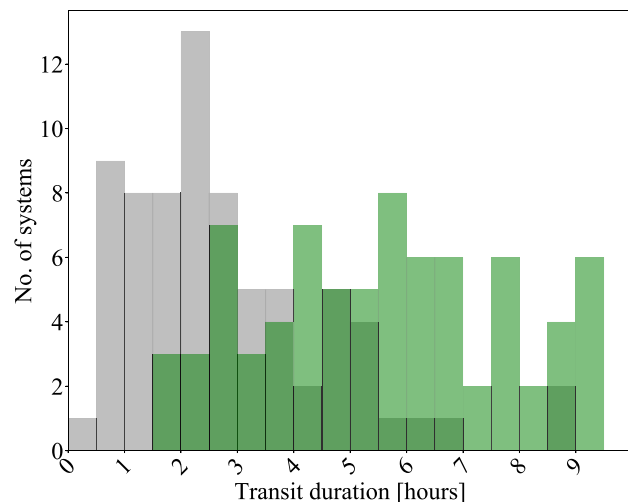
Figure 10. The distribution of transit durations for our duotransit candidates (green) and the confirmed *TESS* discovered exoplanets from the Southern Ecliptic Hemisphere (grey).

would not expect for long-period planets (Gu, Lin & Bodenheimer 2003). Nevertheless, rather than applying an arbitrary upper radius cut, we keep these candidates in our sample for completeness and will rely on follow-up observations to determine the upper radius limit of long-period planets.

Fig. 10 shows that most of our candidates have significantly longer transit durations than many of the confirmed *TESS* planets. This is expected as we are probing planets with orbital periods in excess of ∼17 d, which is significantly longer than the median orbital period of *TESS* planets (∼5.8 d).

In Fig. 11 we plot the *TESS* magnitudes of the host stars of our candidates, again comparing with the sample of confirmed *TESS* planets. Here it can be seen that our long-period planet candidates tend to orbit stars that are significantly fainter than the confirmed planet sample (typically T_{mag} of 10–13). This is for three reasons. First, the confirmed *TESS* sample is biased towards bright stars, partly because brighter stars make it easier to detect shallow transits,

Figure 11. The distribution of *TESS* magnitudes for our duotransit candidate host stars (green) and the confirmed *TESS* discovered exoplanet host stars from the Southern Ecliptic Hemisphere (grey).
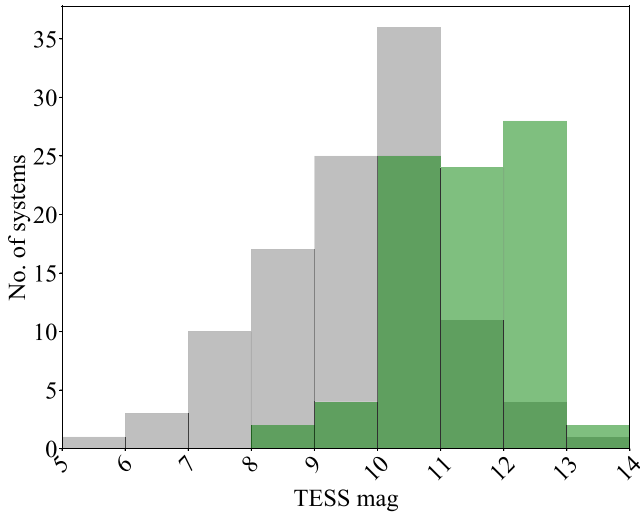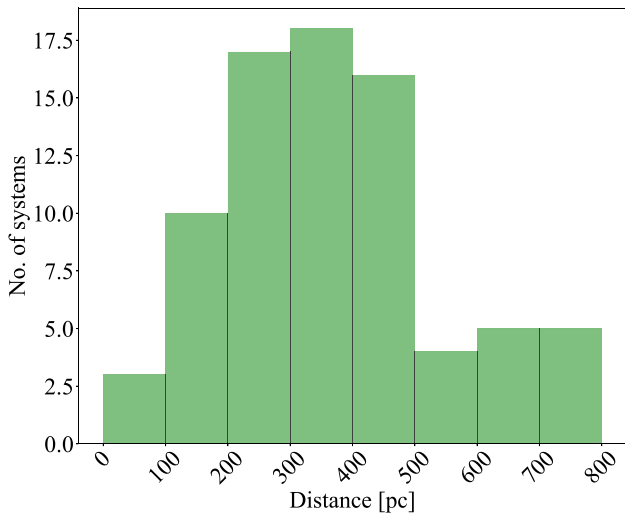

Figure 12. The distribution of *Gaia* DR3 distances (in parsecs) for our duotransit candidate host stars.

and partly because follow-up efforts tend to be focused on bright host stars. Secondly, the much smaller transit probabilities of wide-separation planets means that long-period transiting candidates are rare, and so the brightest detected examples will be around fainter stars, which are more numerous (the absence of brighter examples is not a selection effect because such systems would readily detected). Third, gas giant planets are inherently rarer than the sub-Neptune-sized planets that make up the bulk of the confirmed *TESS* sample. The steep cut-off in our detected candidates at $T_{\mathrm{mag}} = 13$ simply reflects the selection criteria for the SPOC FFI light curves (Caldwell et al. 2020).

In Fig. 12 we plot the distances of our duotransit candidate host stars from the *Gaia* DR3 catalogue. We find that most candidate host stars are at distances from 200–500 pc, with the furthest object being TIC-218977148 at a distance of ~826 pc, and the closest being TIC-303317324/TOI-4310 at a distance of ~40 pc.

As described in Section 3.3, we use the shape and width of our detected transit events to determine the most probable orbital period
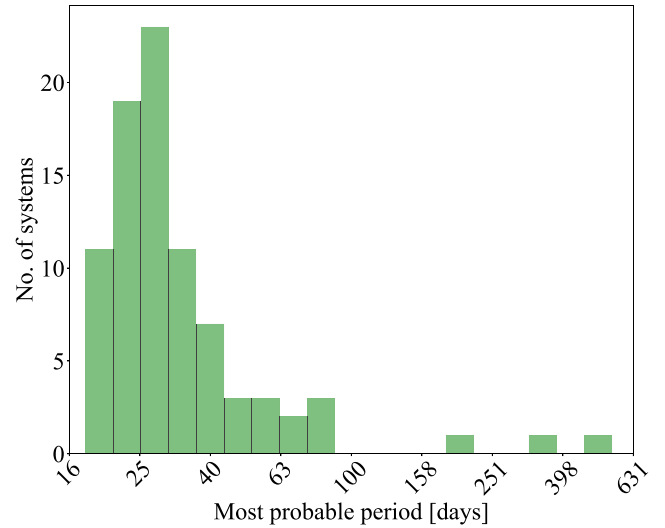
Figure 13. The distribution of most probable periods from modelling with `MonoTools` for our duotransit candidates.

for each candidate (e.g. Osborn et al. 2022). The probability of each allowed alias is indicated on Fig. 4 and the most probable period for each candidate is listed in Table A3. We plot a histogram of these most probable period in Fig. 13. We find that our distribution peaks at periods around 20–30 d. While these values are the most probable periods according to the information and data available, they are not necessarily the correct values, and the true orbital periods must be determined through follow-up observations. We also note the three candidates in our sample with the longest periods: TIC-294097549 with a value of P_{marg} of 200 d, TIC-25194908 with a value of P_{marg} of 338 d, and TIC-349091983 with a value of P_{marg} of 549 d (see Table A3).

5.2 Follow-up programme

5.2.1 Photometric period determination

The limited number of discrete period alias for duotransit candidates means that precise orbital periods can be determined efficiently with photometric follow-up targeted at predicted transit times for each alias.

Our own team is actively following up the duotransit candidates presented here using the Next-Generation Transit Survey (*NGTS*; Wheatley et al. 2018). *NGTS* is a ground-based facility located at the ESO Paranal Observatory in Chile that deploys an array of 12 telescopes optimized for photometric detection of exoplanet transits (e.g. Bryant et al. 2020). Our monotransit programme with *NGTS* confirmed the first planet that was initially identified as a single-transit event with *TESS* (Gill et al. 2020c), and has since confirmed several other long-period planets (e.g. Ulmer-Moll et al. 2022; Grieves et al. 2022, Gill et al., submitted). We have also confirmed three long-period, low-mass eclipsing binary systems (Gill et al. 2020a, b; Lendl et al. 2020).

We are also searching *TESS* Cycle 5 data as they are released for third transits of our duotransit candidates. In some cases this will significantly reduce the number of period aliases to search, although with a similar 2-yr gap between Cycles 1, 3, and 5 a third transit usually still leaves multiple aliases to be searched.

5.2.2 RV detections

Our team has also begun a spectroscopic campaign using the *CORALIE* spectrograph (Queloz et al. 1999) on the Swiss 1.2 m Leonhard Euler Telescope at La Silla Observatory (program ID 500) to help confirm our candidates. With a first *CORALIE* spectrum, we are able to identify and remove double-line spectroscopic binary (SB2) systems, and detect rapidly rotating stars from the broadening of the CCF. With a second *CORALIE* spectrum, taken about one week later, we are able to exclude systems for which the change of measured RV is too large to be consistent with a planetary companion (>1 km s^{-1}). Bright targets hosting relatively massive planetary companions exhibit RV variations detectable with *CORALIE* ($\sim$6 m s^{-1} for bright stars; e.g. Marmier et al. 2013) and for other targets we use *HARPS*. Previous efforts to confirm these mono- and duotransiting planets using spectroscopic observations have been successful (e.g. Grieves et al. 2022; Ulmer-Moll et al. 2022, 2023).

6 CONCLUSION

We have presented the discovery of 85 duotransit candidates from the *TESS*-SPOC FFI light curves from the Southern Ecliptic Hemisphere. The candidates were found using our custom-built `monofind` algorithm through which all SPOC pipeline data products were passed. We also employed a vetting procedure to rule out false-positive scenarios such as eclipsing binaries and asteroids in the sample. A total of 25 of our candidates have previously been flagged as either TOIs or CTOIs, and we found during our vetting process three TOI/CTOI objects outside of our duotransits falsely flagged as such that are asteroids. A dedicated program on the *NGTS* facility is now being used to determine the true orbital periods of these systems, and we welcome other community efforts in this difficult task. We also have programs on instruments such as *CORALIE* and *HARPS* to acquire RV measurements to confirm the planetary nature of these systems and to determine the mass of the exoplanets. Once confirmed, these planets will form the basis for characterization studies into their atmospheric compositions and orbital obliquities, and hence into the formation, evolution, and migration of warm and cool gas giant exoplanets.

DATA AVAILABILITY

The *TESS* data are accessible via the MAST (Mikulski Archive for Space Telescopes) portal at https://mast.stsci.edu/portal/Mashup/Clients/Mast/Portal.html. The associated `python` scripts for analysis and plotting are available upon reasonable request to the authors.

REFERENCES

Akeson R. L. et al., 2013, PASP, 125, 989
Albrecht S. et al., 2012, ApJ, 757, 18
Borucki W. J. et al., 2010, Science, 327, 977
Bryant E. M. et al., 2020, MNRAS, 499, 3139
Bryant E. M., Bayliss D., Van Eylen V., 2023, MNRAS, 521, 3663
Caldwell D. A. et al., 2020, Res. Notes Am. Astron. Soc., 4, 201
Castelli F., Kurucz R. L., 2003, in Piskunov N., Weiss W. W., Gray D. F., eds, Proc. IAU Symp. 210, Modelling of Stellar Atmospheres. Kluwer, Dordrecht, p. A20
Claret A., 2017, A&A, 600, A30
Cooke B. F., Pollacco D., West R., McCormac J., Wheatley P. J., 2018, A&A, 619, A175
Cooke B. F. et al., 2021, MNRAS, 500, 5088
Culpan R., Geier S., Reindl N., Pelisoli I., Gentile Fusillo N., Vorontseva A., 2022, A&A, 662, A40
Dalba P. A. et al., 2020, AJ, 159, 241
Eisner N. L. et al., 2021, MNRAS, 501, 4669
Espinoza N., Jordán A., 2016, MNRAS, 457, 3573
Foreman-Mackey D., Agol E., Ambikasaran S., Angus R., 2017, Astrophysics Source Code Library, record ascl:1709
Foreman-Mackey D. et al., 2021, exoplanet-dev/exoplanet v0.4.5.
Gaia Collaboration, 2022, VizieR Online Data Catalog, I/355
Gill S. et al., 2020a, MNRAS, 491, 1548
Gill S. et al., 2020b, MNRAS, 495, 2713
Gill S. et al., 2020c, ApJ, 898, L11
Grieves N. et al., 2022, A&A, 668, A29
Gu P.-G., Lin D. N. C., Bodenheimer P. H., 2003, ApJ, 588, 509
Han Z., Podsiadlowski P., Maxted P. F. L., Marsh T. R., Ivanova N., 2002, MNRAS, 336, 449
Han Z., Podsiadlowski P., Maxted P. F. L., Marsh T. R., 2003, MNRAS, 341, 669
Hattori S., Foreman-Mackey D., Hogg D. W., Montet B. T., Angus R., Pritchard T. A., Curtis J. L., Schölkopf B., 2022, AJ, 163, 284
Hobson M. J. et al., 2021, AJ, 161, 235
Hsu D. C., Ford E. B., Ragozzine D., Ashby K., 2019, AJ, 158, 109
Jeffery C. S., Miszalski B., Snowdon E., 2021, MNRAS, 501, 623

Jenkins J. M. et al., 2016, in Chiozzi G., Guzman J. C., eds, Proc. SPIE Conf. Ser. Vol. 9913, Software and Cyberinfrastructure for Astronomy IV. SPIE, Bellingham, p. 99133E

Jordán A. et al., 2020, AJ, 159, 145

Kipping D. M., 2013, MNRAS, 434, L51

Kipping D., 2023, MNRAS, 523, 1182

Lendl M. et al., 2020, MNRAS, 492, 1761

Lopez E. D., Fortney J. J., 2016, ApJ, 818, 4

Madhusudhan N., Bitsch B., Johansen A., Eriksson L., 2017, MNRAS, 469, 4102

Marmier M. et al., 2013, A&A, 551, A90

Maxted P. F. L., Heber U., Marsh T. R., North R. C., 2001, MNRAS, 326, 1391

Osborn H. P., 2022, Astrophysics Source Code Library, record ascl:2204.020

Osborn H. P. et al., 2021, MNRAS, 502, 4842

Osborn H. P. et al., 2022, A&A, 664, A156

Pelisoli I., Vos J., Geier S., Schaffenroth V., Baran A. S., 2020, A&A, 642, A180

Queloz D. et al., 1999, preprint(astro-ph/9910223)

Rauch T., Deetjen J. L., 2003, in Hubeny I., Mihalas D., Werner K., eds, ASP Conf. Ser.Vol. 288, Stellar Atmosphere Modeling. Astron. Soc. Pac., San Francisco, p. 103

Rice M. et al., 2022, AJ, 164, 104

Ricker G. R. et al., 2015, J. Astron. Tel. Instrum. Syst., 1, 014003

Salvatier J., Wiecki T. V., Fonnesbeck C., 2016, PeerJ Comput. Sci., 2, e55

Schaffenroth V., Pelisoli I., Barlow B. N., Geier S., Kupfer T., 2022, A&A, 666, A182

Schlecker M. et al., 2020, AJ, 160, 275

Seabroke G. M. et al., 2021, A&A, 653, A160

Smith J. C. et al., 2012, PASP, 124, 1000

Stark M. A., Wade R. A., 2003, AJ, 126, 1455

Stassun K. G. et al., 2019, AJ, 158, 138

Stumpe M. C. et al., 2012, PASP, 124, 985

Stumpe M. C., Smith J. C., Catanzarite J. H., Van Cleve J. E., Jenkins J. M., Twicken J. D., Girouard F. R., 2014, PASP, 126, 100

Temple L. Y. et al., 2018, MNRAS, 480, 5307

Temple L. Y. et al., 2019, MNRAS, 490, 2467

Thuillier A., Van Grootel V., Dévora-Pajares M., Pozuelos F. J., Charpinet S., Siess L., 2022, A&A, 664, A113

Twicken J. et al., 2019, American Astronomical Society Meeting Abstracts, Vol. 233. p. 140.03

Ulmer-Moll S. et al., 2022, A&A, 666, A46

Ulmer-Moll S. et al., 2023, A&A, 674, A43

Van Grootel V. et al., 2021, A&A, 650, A205

Villanueva, Steven J., Dragomir D., Gaudi B. S., 2019, AJ, 157, 84

Vos J., Vučković M., Chen X., Han Z., Boudreaux T., Barlow B. N., Østensen R., Németh P., 2019, MNRAS, 482, 4592

Wang S. et al., 2021, AJ, 162, 50

Watson C. A., de Mooij E. J. W., Steeghs D., Marsh T. R., Brogi M., Gibson N. P., Matthews S., 2019, MNRAS, 490, 1991

Werner K., Dreizler S., 1999, J. Comput. Appl. Math., 109, 65

Werner K., Deetjen J. L., Dreizler S., Nagel T., Rauch T., Schuh S. L., 2003, in Hubeny I., Mihalas D., Werner K., eds, ASP Conf. Ser. Vol. 288, Stellar Atmosphere Modeling. Astron. Soc. Pac., San Francisco, p. 31

Wheatley P. J. et al., 2018, MNRAS, 475, 4476

APPENDIX A: CANDIDATES AND LIGHT CURVES

Table A1. Properties of the host stars of our duotransit candidates.

ID	TIC ID	TOI/CTOI	RA (deg)	Dec (deg)	T_{mag}	$R_\star$ ($R_\odot$)	T_{eff} (K)	Distance (pc)	N_{sec}
1	1504460	–	131.9658	−23.9895	11.63	1.5	6218	$451.71^{+20.73}_{-15.90}$	2
2	2669681	–	289.368	−28.5803	11.47	1.88	5160	$382.06^{+12.79}_{-9.96}$	2
3	9844069	–	48.03923	−11.6808	12.96	1.61	5665	$777.93^{+11.74}_{-11.59}$	2
4	13072758	CTOI	76.08837	−29.0342	12.22	1.43	6313	$601.42^{+2.95}_{-3.19}$	2
5	13713700	–	133.6396	−7.94134	12.29	0.97	5864	$391.66^{+2.67}_{-2.25}$	2
6	14445414	–	110.8209	12.66321	11.02	1.31	6425	$346.17^{+12.45}_{-3.76}$	2
7	20904104	–	7.41368	−19.3663	9.76	0.88	5628	$105.79^{+0.24}_{-0.22}$	2
8	25194908	–	63.90318	−66.3519	12.46	1.32	6309	$666.61^{+32.34}_{-8.91}$	24
9	32179255	–	332.0396	−29.6093	10.52	1.75	5989	$330.44^{+14.95}_{-7.29}$	2
10	38138512	–	170.4183	−4.19721	12.94	1.34	6300	$769.66^{+10.80}_{-9.15}$	2
11	39167176	–	88.32738	−3.79767	12.01	1.56	8416	$486.84^{+3.95}_{-1.46}$	2
12	42428568	–	96.29347	−3.76657	10.83	2.16	6686	$567.87^{+8.12}_{-10.63}$	2
13	52195587	–	19.24834	−66.1636	12.25	1.2	5736	$450.99^{+2.50}_{-2.59}$	4
14	66439839	–	14.47851	−30.3231	11.97	1.03	5882	$356.25^{+2.47}_{-3.35}$	3
15	67599025	CTOI	17.69268	−31.5055	11.96	0.78	4816	$177.82^{+1.19}_{-1.34}$	2
16	70561926	–	139.2559	−26.7007	11	1.35	6386	$353.55^{+5.09}_{-3.76}$	2
17	71028120	–	66.12741	−11.9835	10.44	1.37	5596	$215.31^{+0.82}_{-0.84}$	2
18	77437543	TOI-2490	73.12441	−36.2572	11.28	1.17	5459	$264.92^{+1.04}_{-0.96}$	3
19	81089255	CTOI	122.6942	−43.8535	11.84	1.43	7459	$547.70^{+2.71}_{-2.72}$	4
20	100776118	CTOI	88.31784	−34.5185	11.51	1.25	6439		4
21	101824521	–	206.004	−26.4978	12.61	1.23	5553	$481.79^{+4.21}_{-3.97}$	2
22	107113345	–	183.0341	−32.6628	10.34	1.31	6696	$267.74^{+1.41}_{-1.63}$	2
23	118339710	CTOI	129.572	−23.5502	10.35	1.56	6119	$285.48^{+15.23}_{-4.22}$	3
24	123763494	–	90.30269	−21.2359	11.73	1.22	5568	$353.10^{+29.67}_{-9.36}$	2
25	124029677	TOI-5153	91.54028	−19.9533	11.21	1.38	6408	$366.92^{+2.94}_{-2.71}$	2

Table A1 – *continued*

ID	TIC ID	TOI/CTOI	RA (deg)	Dec (deg)	T_{mag}	$R_\star$ ($R_\odot$)	T_{eff} (K)	Distance (pc)	N_{sec}
26	140215502	CTOI	85.15071	−34.7664	11.23	0.93	5528	$210.03^{+0.62}_{-0.56}$	4
27	140750416	–	116.4382	−23.143	11.81	0.87	5331	$238.74^{+5.45}_{-2.41}$	2
28	142278054	–	180.7626	−33.343	10.28	2.39	6400	$418.42^{+1.64}_{-2.10}$	2
29	145006304	–	193.3345	−39.7347	11.3	1.12	6340	$309.68^{+1.88}_{-1.72}$	2
30	145913596	–	123.1298	−30.5555	10.17	1.45	6467	$261.13^{+1.63}_{-0.99}$	4
31	153838604	–	68.07396	−47.6088	12.48	0.91	5649	$387.07^{+22.34}_{-7.33}$	4
32	156716001	–	103.1063	−39.6876	10.9	1.08	6129	$240.55^{+2.60}_{-11.28}$	4
33	157119927	–	175.2155	−31.1374	11.64	1.04	5765	$299.69^{+8.62}_{-2.98}$	2
34	157698565	TOI-2589	107.4883	−37.231	10.72	1.07	5938	$198.90^{+23.29}_{-1.84}$	3
35	159490807	–	220.2349	−39.3757	10.57	1.69	6556	$341.73^{+3.68}_{-3.50}$	2
36	161169240	CTOI	339.3573	−53.3188	12.12	1.19	5952	$445.30^{+6.33}_{-36.66}$	2
37	176518126	–	87.1832	−0.49503	10.48	1.36	7927	$281.19^{+1.57}_{-1.56}$	2
38	188620407	CTOI	350.0511	−13.0494	11.57	1.31	6169	$404.71^{+3.12}_{-2.81}$	3
39	193318850	–	177.7302	−16.7417	12.76	0.79	5560	$340.21^{+1.78}_{-1.68}$	2
40	207783865	–	207.0609	−54.4206	10.54	1.04	5936	$180.65^{+2.63}_{-0.98}$	2
41	211409161	–	321.7768	−30.5273	10.44	0.78	4660		2
42	215402824	–	43.0624	−36.2887	12.97	1.33	6180	$761.55^{+11.13}_{-8.01}$	4
43	218977148	–	349.5331	−33.1369	12.58	1.61	6214	$826.08^{+12.07}_{-12.51}$	2
44	220622886	–	84.89306	−42.6811	12	2.56	5671	$796.01^{+3.48}_{-16.0}$	3
45	221915858	–	249.513	−54.3579	10.07	2.47	9475		2
46	224279805	CTOI	355.7386	−40.7722	12.15	1.2	5591	$422.59^{+3.22}_{-3.1}$	2
47	235058563	–	83.51699	−50.1216	12.43	1.47	6438	$706.77^{+5.66}_{-5.64}$	6
48	237605045	–	103.2896	2.05465	10.29	2.92	6577	$471.34^{+7.62}_{-7.43}$	2
49	242241304	CTOI	211.5851	−43.0447	11.81	1.14	5781	$346.35^{+1.79}_{-1.77}$	2
50	251057075	–	36.17507	−5.85401	11.05	0.84	5225	$157.35^{+0.52}_{-0.54}$	2
51	256912435	–	200.5462	−55.2184	11.8	1.19	5650	$333.69^{+3.17}_{-3.45}$	2
52	265465927	CTOI	320.9166	−62.9238	12.08	1.16	6099	$418.77^{+65.41}_{-56.26}$	2
53	265466589	–	321.0794	−64.4743	12.61	1.03	5834		2
54	268534931	CTOI	15.12618	−23.1795	12.22	0.78	5179	$246.72^{+7.21}_{-2.25}$	2
55	269333648	TOI-2529	118.9944	−52.3549	10.67	1.75	5822	$295.40^{+2.04}_{-1.85}$	6
56	275878706	–	207.9018	−44.3144	12.17	0.93	5038	$247.70^{+2.42}_{-2.18}$	2
57	279727635	–	50.59176	−64.4444	12.5	1.05	5851	$447.75^{+3.66}_{-3.51}$	6
58	287204963	–	30.28722	−11.8835	13.25	1.04	5344	$551.78^{+10.06}_{-5.87}$	2
59	289840544	–	317.5455	−26.3999	10.64	1.75	5989	$329.46^{+3.72}_{-3.65}$	2
60	290165539	–	319.8521	−25.5971	11.99	1.33	5895	$453.86^{+6.32}_{-15.61}$	2
61	292719109	–	107.416	3.56756	10.1	2.08	6216	$326.24^{+9.07}_{-9.63}$	2
62	294097549	–	107.67	−55.7967	10.47	1.15	5872	$197.78^{+0.46}_{-0.5}$	13
63	296737508	CTOI	142.1793	−14.6864	9.2	1.27	5700	$117.37^{+0.23}_{-0.22}$	2
64	300394149	–	170.747	−52.6986	10.13	1.42	5997	$218.59^{+0.60}_{-0.59}$	2
65	303317324	TOI-4310	351.9037	−25.5081	9.5	0.72	4159	$40.13^{+0.43}_{-0.10}$	2
66	304339227	TOI-4629	275.9439	−68.3449	8.66	1.13	6012	$91.13^{+0.23}_{-0.15}$	2
67	306249066	–	166.7285	−54.7388	10.54	1.14	6139	$221.63^{+1.01}_{-2.35}$	2
68	313671132	–	202.1582	−62.1699	10.08	1.22	5878	$175.65^{+0.41}_{-0.43}$	2
69	317923092	–	89.85183	−14.9061	12.26	1.34	7604	$668.65^{+21.27}_{-10.4}$	2
70	323295479	TOI-1861	130.7987	−83.061	9.95	1.06	5684	$134.32^{+0.24}_{-0.23}$	5
71	332697924	–	63.26121	−12.4593	11	1.32	6266	$312.19^{+3.28}_{-9.2}$	2
72	333736132	CTOI	170.2765	−26.0666	12.07	0.76	4722	$178.23^{+0.58}_{-1.38}$	2
73	339399841	–	296.0705	−62.8136	12.35	1.55	5686	$596.49^{+4.8}_{-5.11}$	2
74	349091983	–	107.7051	−61.3524	12.29	1.5	6083		24
75	381553868	–	269.7743	−50.9212	11.85	1.59	6355		2
76	393229954	–	86.74486	−46.7119	11.77	0.9	5571	$262.19^{+5.47}_{-1.15}$	5

Table A1 – *continued*

ID	TIC ID	TOI/CTOI	RA (deg)	Dec (deg)	T_{mag}	$R_\star$ ($R_\odot$)	T_{eff} (K)	Distance (pc)	N_{sec}
77	394340183	–	39.32208	−79.4583	10.95	1.04	6325	$253.84^{+0.64}_{-0.65}$	2
78	396720998	TOI-709	65.65532	−54.1472	13.99	0.15	50 000		6
79	404518509	TOI-4320	51.64036	−43.6136	8.6	1.04	5871	$79.30^{+0.07}_{-0.07}$	4
80	412386707	–	110.4871	−23.414	10.92	1.96	6304	$425.23^{+5.01}_{-4.39}$	2
81	437293313	–	191.2234	−22.6177	12.97	0.94	5536	$416.28^{+7.26}_{-6.35}$	2
82	439491923	–	21.38365	−18.1471	12.87	1.26	5944	$631.09^{+11.04}_{-9.74}$	2
83	442893494	–	80.00938	−16.2193	12.41	1.39	6322	$622.15^{+5.22}_{-5.04}$	3
84	457649900	TOI-4958	217.9991	−51.0744	10.75	2.11	6713	$479.53^{+4.71}_{-3.72}$	2
85	466206508	TOI-5542	302.7985	−61.1355	11.85	1.27	5393	$342.66^{+1.69}_{-1.51}$	2

Table A2. The transit event properties of our duotransit candidates.

ID	TIC ID	T_{c1}	T_{c2}	Depth	Duration
–	–	(TBJD, [Sector])	(TBJD, [Sector])	(ppt)	(h)
1	1504460	1528.39739 [08]	2261.11990 [35]	3.367 [08], 3.415 [35]	3.78
2	2669681	1676.73302 [13]	2044.45589 [27]	7.879 [13], 7.037 [27]	9.69
3	9844069	1431.16511 [04]	2148.92146 [31]	13.452 [04], 12.224 [31]	7.20
4	13072758	1455.59404 [05]	2193.21295 [32]	7.023 [05], 6.755 [32]	9.25
5	13713700	1536.98226 [08]	2245.82903 [34]	7.234 [08], 4.700 [34]	3.26
6	14445414	1497.55590 [07]	2210.97620 [33]	2.317 [07], 2.179 [33]	2.86
7	20904104	1390.11189 [03]	2105.36177 [29]	0.738 [03], 1.065 [29]	4.61
8	25194908	1402.29491 [03]	2077.28343 [28]	6.590 [03], 6.266 [28]	9.16
9	32179255	1345.87922 [01]	2068.45418 [28]	3.619 [01], 4.682 [28]	3.71
10	38138512	1559.95080 [09]	2300.02560 [36]	17.907 [09], 18.148 [36]	6.73
11	39167176	1470.62312 [06]	2211.42630 [33]	7.282 [06], 8.112 [33]	6.25
12	42428568	1475.69109 [06]	2224.32460 [33]	5.380 [06], 4.939 [33]	10.20
13	52195587	1350.27811 [01]	2107.61083 [29]	5.775 [01], 6.138 [29]	9.07
14	66439839	1386.34406 [03]	2137.03203 [30]	6.227 [03], 5.420 [30]	2.16
15	67599025	1404.02101 [03]	2138.82557 [30]	6.684 [03], 7.345 [30]	3.27
16	70561926	1523.06353 [08]	2275.36040 [35]	16.290 [08], 16.053 [35]	5.91
17	71028120	1445.81123 [05]	2189.95412 [32]	1.238 [05], 1.025 [32]	6.11
18	77437543	1456.70241 [05]	2180.69226 [32]	9.825 [05], 9.326 [32]	7.93
19	81089255	1509.94498 [07]	2260.20690 [35]	7.318 [07], 6.372 [35]	5.14
20	100776118	1472.81029 [06]	2219.67770 [33]	13.264 [06], 13.070 [33]	22.34
21	101824521	1620.35423 [11]	2331.52820 [37]	9.396 [11], 9.103 [37]	8.52
22	107113345	1576.32832 [10]	2317.29675 [37]	1.771 [10], 2.035 [37]	1.77
23	118339710	1525.64667 [08]	2249.54641 [34]	4.329 [08], 3.977 [34]	8.68
24	123763494	1486.92891 [06]	2209.76758 [33]	10.645 [06], 11.728 [33]	2.47
25	124029677	1486.12090 [06]	2218.00409 [33]	6.368 [06], 6.105 [33]	4.58
26	140215502	1460.54584 [05]	2194.44033 [32]	2.959 [05], 4.468 [32]	7.14
27	140750416	1504.80151 [07]	2245.39501 [34]	8.912 [07], 9.197 [34]	3.85
28	142278054	1595.02504 [10]	2310.35369 [37]	2.177 [10], 2.022 [37]	4.82
29	145006304	1579.50384 [10]	2318.24443 [37]	2.048 [10], 2.772 [37]	5.19
30	145913596	1539.51696 [08]	2242.69675 [34]	1.728 [08], 2.163 [34]	8.50
31	153838604	1447.10227 [05]	2176.13853 [32]	15.209 [05], 16.237 [32]	2.61
32	156716001	1485.40631 [06]	2224.51833 [33]	2.652 [06], 3.037 [33]	9.11
33	157119927	1591.62175 [10]	2291.00613 [36]	5.445 [10], 6.897 [36]	2.57
34	157698565	1494.57973 [07]	2234.11360 [34]	9.825 [07], 9.338 [34]	6.38
35	159490807	1606.22551 [11]	2355.93796 [38]	5.155 [11], 5.184 [38]	5.38
36	161169240	1328.25945 [01]	2083.31754 [28]	9.707 [01], 10.134 [28]	7.82
37	176518126	1489.05533 [06]	2219.53761 [33]	3.565 [06], 3.244 [33]	5.61
38	188620407	1375.48660 [02]	2461.70715 [42]	5.467 [02], 4.512 [42]	6.08
39	193318850	1553.77031 [09]	2292.51011 [36]	6.916 [09], 7.143 [36]	3.89
40	207783865	1608.93692 [11]	2354.11345 [38]	17.211 [11], 17.729 [38]	1.99
41	211409161	1335.10057 [01]	2070.36583 [28]	13.629 [01], 12.232 [28]	2.14
42	215402824	1413.62655 [04]	2169.04205 [31]	5.589 [04], 9.955 [31]	1.87
43	218977148	1355.47069 [02]	2090.09772 [29]	5.597 [02], 4.944 [29]	8.13
44	220622886	1479.52544 [06]	2204.58502 [33]	4.324 [06], 3.501 [33]	4.43
45	221915858	1643.35799 [12]	2372.55118 [39]	5.737 [12], 5.526 [39]	3.05

Table A2 – *continued*

ID	TIC ID	T_c1 (TBJD, [Sector])	T_c2 (TBJD, [Sector])	Depth (ppt)	Duration (h)
–	–				
46	224279805	1369.72941 [02]	2105.21571 [29]	6.392 [02], 6.618 [29]	5.93
47	235058563	1416.61066 [04]	2216.44259 [33]	6.164 [04], 5.630 [33]	10.17
48	237605045	1489.04268 [06]	2210.29724 [33]	6.212 [06], 7.014 [33]	4.42
49	242241304	1623.07095 [11]	2345.37403 [38]	6.158 [11], 6.186 [38]	4.72
50	251057075	1426.31846 [04]	2154.02335 [31]	1.986 [04], 2.348 [31]	4.42
51	256912435	1623.43775 [11]	2338.70979 [38]	20.396 [11], 21.562 [38]	2.72
52	265465927	1342.64749 [01]	2058.60913 [27]	8.678 [01], 8.720 [27]	6.05
53	265466589	1352.52439 [01]	2037.86660 [27]	6.818 [01], 6.664 [27]	4.14
54	268534931	1398.29475 [03]	2139.09941 [30]	5.829 [03], 6.133 [30]	7.82
55	269333648	1538.52419 [08]	2249.05416 [34]	4.162 [08], 4.032 [34]	9.46
56	275878706	1621.08010 [11]	2341.78257 [38]	6.544 [11], 5.320 [38]	4.38
57	279727635	1343.22676 [01]	2124.62930 [30]	7.181 [01], 6.789 [30]	5.71
58	287204963	1402.93640 [03]	2132.33438 [30]	11.498 [03], 10.182 [30]	4.73
59	289840544	1331.28977 [01]	2083.28790 [28]	2.702 [01], 1.997 [28]	2.99
60	290165539	1332.75615 [01]	2067.97094 [28]	13.627 [01], 15.056 [28]	11.50
61	292719109	1499.70159 [07]	2222.31933 [33]	2.859 [07], 2.677 [33]	9.08
62	294097549	1657.74149 [13]	2256.34250 [35]	1.977 [13], 1.426 [35]	7.96
63	296737508	1538.00622 [08]	2271.99796 [35]	2.021 [08], 1.854 [35]	5.65
64	300394149	1576.88642 [10]	2325.42588 [37]	2.051 [10], 2.195 [37]	13.40
65	303317324	1365.17582 [02]	2104.34337 [29]	1.360 [02], 1.323 [29]	5.74
66	304339227	1673.33918 [13]	2388.01911 [39]	0.522 [13], 0.464 [39]	5.79
67	306249066	1593.97611 [10]	2326.51397 [37]	7.873 [10], 7.061 [37]	4.03
68	313671132	1604.35452 [11]	2337.72693 [38]	3.408 [11], 3.506 [38]	5.70
69	317923092	1479.81772 [06]	2209.42617 [33]	4.358 [06], 6.715 [33]	12.96
70	323295479	1622.92483 [11]	2365.44036 [39]	8.727 [11], 8.609 [39]	6.51
71	332697924	1445.74977 [05]	2178.22194 [32]	1.042 [05], 1.423 [32]	6.63
72	333736132	1551.55292 [09]	2283.54681 [36]	15.856 [09], 16.440 [36]	2.96
73	339399841	1662.10984 [13]	2043.59486 [27]	4.773 [13], 6.471 [27]	6.66
74	349091983	1603.10253 [11]	2152.16754 [31]	8.301 [11], 8.133 [31]	9.52
75	381553868	1677.32594 [13]	2367.57869 [39]	5.653 [13], 6.030 [39]	6.49
76	393229954	1446.79953 [05]	2204.55168 [33]	8.172 [05], 6.652 [33]	2.67
77	394340183	1664.84261 [13]	2389.11243 [39]	11.255 [13], 10.820 [39]	8.65
78	396720998	1399.21966 [03]	2176.27178 [30]	6.360 [03], 6.082 [30]	4.33
79	404518509	1431.26615 [04]	2134.88294 [30]	0.842 [04], 0.598 [30]	5.02
80	412386707	1493.95365 [07]	2240.57066 [34]	3.442 [07], 3.587 [34]	5.23
81	437293313	1578.44737 [10]	2328.08914 [37]	9.891 [10], 8.462 [37]	6.58
82	439491923	1405.41115 [03]	2116.79038 [30]	11.608 [03], 11.766 [30]	6.70
83	442893494	1472.65885 [06]	2194.38454 [32]	5.776 [06], 6.458 [32]	7.70
84	457649900	1606.96984 [11]	2355.79522 [38]	2.857 [11], 2.945 [38]	7.61
85	466206508	1679.34576 [13]	2054.97133 [27]	11.214 [13], 9.274 [27]	8.03

Table A3. Properties of our duotransit candidates. N_{alias} is the alias number corresponding to the most probable orbital period P_{marg}.

ID	TIC ID	R_p ($R_\oplus$)	P_{min}, P_{max} (d)	N_{alias}	P_{marg} (d)	b	Gaia NSS	Gaia RV amp (km s^{-1})	Total SNR
1	1504460	9.6 ± 1.0	19.80333, 732.72251	24	$20.0^{+19.0}_{-1.0}$	$0.78^{+0.12}_{-0.37}$	0	13.84	14.82
2	2669681	17.0 ± 1.2	21.63067, 367.72287	18	$24.5^{+8.9}_{-2.9}$	$0.66^{+0.09}_{-0.24}$	0	36.15	41.8
3	9844069	18.9 ± 1.4	22.42991, 717.75635	33	$25.6^{+7.0}_{-3.2}$	$0.62^{+0.12}_{-0.3}$	0	–	46.12
4	13072758	$11.78^{+0.67}_{-0.65}$	19.93567, 737.61891	38	26.0 ± 10.0	0.31 ± 0.22	0	20.36	35.92
5	13713700	8.3 ± 1.0	19.69018, 708.84677	37	$22.9^{+8.0}_{-3.2}$	$0.79^{+0.11}_{-0.28}$	0	–	19.73
6	14445414	$7.5^{+3.9}_{-1.2}$	19.28163, 713.42031	38	$22.3^{+7.4}_{-3.0}$	$0.93^{+0.06}_{-0.18}$	0	4.78	12.08
7	20904104	2.6 ± 0.19	17.88103, 715.24989	41	$23.0^{+11.0}_{-4.0}$	$0.27^{+0.25}_{-0.19}$	0	2.9	11.84
8	25194908	11.18 ± 0.68	337.49490, 674.98980	2	337.49490	$0.7^{+0.1}_{-0.28}$	0	–	31.43
9	32179255	21.0 ± 8.0	20.64500, 722.57496	36	$22.6^{+6.3}_{-1.9}$	$0.999^{+0.07}_{-0.045}$	2	49.01	36.77
10	38138512	17.8 ± 1.0	18.50185, 740.07480	41	$21.1^{+6.3}_{-2.2}$	0.32 ± 0.2	0	–	49.35
11	39167176	$18.8^{+8.9}_{-2.9}$	20.57787, 740.80317	37	$26.0^{+20.0}_{-5.0}$	$0.947^{+0.081}_{-0.044}$	0	81.59	40.79
12	42428568	$24.0^{+11.0}_{-5.0}$	24.14954, 748.63351	32	$31.0^{+22.0}_{-6.0}$	$0.981^{+0.066}_{-0.038}$	0	16.42	56.65
13	52195587	9.28 ± 0.52	34.42428, 757.33272	18	50.0 ± 17.0	0.29 ± 0.22	0	–	35.19
14	66439839	$9.1^{+2.8}_{-1.0}$	37.53440, 750.68798	17	$38.0^{+20.0}_{-2.0}$	$0.87^{+0.09}_{-0.29}$	0	30.94	19.55
15	67599025	6.86 ± 0.57	24.49349, 734.80456	31	$27.2^{+7.8}_{-2.7}$	$0.62^{+0.13}_{-0.35}$	0	9.86	29.54
16	70561926	17.51 ± 0.82	20.33234, 752.29687	38	$22.1^{+5.7}_{-1.8}$	0.15 ± 0.12	2	18.35	144.8
17	71028120	4.74 ± 0.31	18.60345, 744.14289	41	$21.3^{+6.3}_{-2.7}$	$0.38^{+0.22}_{-0.25}$	0	2.53	14.28
18	77437543	$10.98^{+0.66}_{-0.63}$	22.62465, 723.98986	22	$38.0^{+14.0}_{-15.0}$	0.31 ± 0.22	2	14.02	83.13
19	81089255	12.19 ± 0.69	34.10282, 750.26191	23	$37.5^{+9.4}_{-4.9}$	$0.76^{+0.07}_{-0.26}$	0	24.24	25.14
20	100776118	16.19 ± 0.74	49.79069, 746.86040	16	$62.0^{+31.0}_{-12.0}$	0.842 ± 0.01	3	30.51	177.47
21	101824521	12.17 ± 0.72	24.52324, 711.17397	30	31.0 ± 10.0	$0.18^{+0.18}_{-0.13}$	0	–	34.34
22	107113345	$9.2^{+5.1}_{-2.3}$	20.02618, 740.96843	38	$22.5^{+6.0}_{-2.4}$	0.976 ± 0.048	0	19.1	12.5
23	118339710	$10.64^{+0.65}_{-0.61}$	21.29118, 723.89974	26	33.0 ± 12.0	0.48 ± 0.29	0	4.13	62.67
24	123763494	$19.8^{+7.1}_{-4.5}$	19.53618, 722.83868	38	$21.9^{+5.9}_{-2.4}$	$0.97^{+0.076}_{-0.062}$	0	15.94	37.36
25	124029677	11.35 ± 0.59	18.76624, 731.88319	40	$20.9^{+5.2}_{-2.1}$	$0.43^{+0.22}_{-0.28}$	0	11.35	46.16
26	140215502	$5.78^{+0.38}_{-0.34}$	34.94727, 733.89270	22	$43.0^{+18.0}_{-8.0}$	$0.31^{+0.3}_{-0.21}$	0	9.83	32.98
27	140750416	8.55 ± 0.54	16.83165, 740.59260	45	$19.0^{+4.9}_{-2.2}$	0.36 ± 0.22	0	11.19	30.13
28	142278054	$11.49^{+0.96}_{-0.91}$	24.66649, 715.32865	30	$27.5^{+6.6}_{-2.8}$	$0.79^{+0.11}_{-0.38}$	0	7.72	23.25
29	145006304	$5.33^{+0.47}_{-0.43}$	16.78954, 738.74000	45	$18.9^{+5.7}_{-2.2}$	$0.62^{+0.17}_{-0.35}$	0	6.03	13.84
30	145913596	$6.9^{+2.7}_{-1.1}$	54.09067, 703.17978	14	$59.0^{+29.0}_{-8.0}$	$0.91^{+0.07}_{-0.32}$	0	5.83	25.32
31	153838604	$17.1^{+4.7}_{-3.3}$	38.37032, 729.03626	20	$41.0^{+12.0}_{-4.0}$	$0.961^{+0.068}_{-0.062}$	0	–	42.87
32	156716001	5.97 ± 0.3	33.59600, 739.11201	23	$43.0^{+30.0}_{-10.0}$	0.28 ± 0.22	0	4.73	33.42
33	157119927	$13.4^{+5.9}_{-3.1}$	21.19346, 699.38439	34	$24.1^{+6.3}_{-2.9}$	$0.983^{+0.071}_{-0.048}$	2	64.82	25.01
34	157698565	11.66 ± 0.59	35.21588, 739.53387	22	$46.0^{+28.0}_{-11.0}$	$0.827^{+0.025}_{-0.041}$	0	3.49	105.68
35	159490807	$15.4^{+4.7}_{-1.6}$	22.71853, 749.71245	34	29.0 ± 8.0	$0.938^{+0.048}_{-0.025}$	0	6.08	45.05
36	161169240	$12.19^{+0.77}_{-0.73}$	26.03638, 755.05809	30	$31.0^{+13.0}_{-4.0}$	$0.47^{+0.21}_{-0.29}$	0	32.37	52.27
37	176518126	8.3 ± 1.1	21.48477, 730.48210	35	$24.3^{+7.4}_{-2.9}$	0.3 ± 0.22	0	9.38	32.89
38	188620407	$9.58^{+0.57}_{-0.54}$	24.13819, 1086.21870	35	28.0 ± 10.0	0.39 ± 0.24	0	11.56	33.51
39	193318850	7.08 ± 0.47	15.07635, 738.73979	50	$17.6^{+5.5}_{-2.2}$	0.31 ± 0.22	0	–	17.05
40	207783865	15.31 ± 0.76	21.29077, 745.17689	36	$23.3^{+6.5}_{-2.0}$	$0.802^{+0.023}_{-0.035}$	2	13.91	95.83
41	211409161	$13.1^{+4.5}_{-2.6}$	18.85295, 735.26527	40	$21.0^{+5.3}_{-2.2}$	$0.943^{+0.077}_{-0.066}$	0	38.64	38.49
42	215402824	$16.0^{+10.0}_{-3.0}$	41.96752, 755.41550	16	$42.0^{+21.0}_{-2.0}$	$0.93^{+0.11}_{-0.22}$	0	–	12.73
43	218977148	11.9 ± 0.82	27.20845, 734.62703	28	$30.6^{+8.1}_{-3.4}$	$0.4^{+0.22}_{-0.26}$	0	–	22.83
44	220622886	$28.0^{+16.0}_{-8.0}$	42.65054, 725.05958	18	$29.0^{+23.0}_{-0.0}$	$0.994^{+0.071}_{-0.048}$	0	65.91	18.89
45	221915858	$21.3^{+3.7}_{-1.4}$	17.78520, 729.19319	42	$19.7^{+5.4}_{-1.9}$	$0.911^{+0.044}_{-0.025}$	0	60.96	33.79
46	224279805	10.55 ± 0.64	17.51161, 735.48631	43	$19.9^{+5.5}_{-1.9}$	0.24 ± 0.18	0	17.77	30.43
47	235058563	11.47 ± 0.61	88.87019, 799.83193	10	$89.0^{+25.0}_{-9.0}$	0.38 ± 0.23	0	–	27.17
48	237605045	$44.0^{+17.0}_{-11.0}$	21.85618, 721.25400	34	$24.0^{+6.0}_{-2.2}$	$1.01^{+0.067}_{-0.051}$	0	36.88	68.84
49	242241304	9.7 ± 1.0	23.30012, 722.30308	32	$28.0^{+10.0}_{-4.0}$	$0.855^{+0.061}_{-0.071}$	0	7.03	28.72
50	251057075	3.88 ± 0.3	16.53870, 727.70489	45	$20.2^{+7.8}_{-3.3}$	0.27 ± 0.22	0	7.82	15.54
51	256912435	$25.5^{+4.6}_{-3.8}$	24.66455, 715.27204	30	$27.5^{+6.6}_{-2.8}$	0.95 ± 0.051	0	46.85	57.7
52	265465927	11.73 ± 0.63	23.86539, 715.96164	31	$27.5^{+8.3}_{-3.7}$	0.27 ± 0.19	0	19.67	38.93
53	265466589	8.57 ± 0.59	28.55588, 685.34120	25	$31.2^{+9.2}_{-3.7}$	$0.49^{+0.21}_{-0.33}$	0	–	13.71
54	268534931	6.12 ± 0.39	24.69345, 740.80465	31	$32.0^{+25.0}_{-7.0}$	0.29 ± 0.23	0	25.23	29.74
55	269333648	11.72 ± 0.67	64.59377, 710.52997	12	$65.0^{+24.0}_{-5.0}$	$0.64^{+0.1}_{-0.25}$	0	3.2	54.46

Table A3 – *continued*

ID	TIC ID	R_p	P_{min}, P_{max}	N_{alias}	P_{marg}	b	*Gaia*	*Gaia* RV	Total SNR
–	–	$(R_\oplus)$	(d)	–	(d)	–	NSS	amp (km s^{-1})	–
56	275878706	$8.1^{+3.1}_{-1.3}$	22.52196, 720.70247	33	$27.0^{+11.0}_{-4.0}$	$0.88^{+0.09}_{-0.21}$	1	21.81	20.68
57	279727635	$10.5^{+4.0}_{-1.2}$	65.11699, 781.40254	13	$71.0^{+41.0}_{-19.0}$	0.905 ± 0.078	0	–	28.36
58	287204963	11.3 ± 2.2	17.79021, 729.39798	42	$20.3^{+5.8}_{-2.5}$	$0.41^{+0.25}_{-0.28}$	0	–	17.86
59	289840544	$14.0^{+9.1}_{-3.6}$	22.78782, 751.99813	34	$25.1^{+6.3}_{-2.3}$	$0.984^{+0.063}_{-0.045}$	0	6.43	17.85
60	290165539	$23.4^{+6.3}_{-3.4}$	21.62396, 735.21479	35	$27.0^{+19.0}_{-5.0}$	$0.95^{+0.066}_{-0.046}$	0	45.38	92.47
61	292719109	11.07 ± 0.59	21.89747, 722.61775	34	$24.1^{+7.3}_{-2.2}$	0.34 ± 0.23	0	2.5	45.22
62	294097549	4.79 ± 0.33	199.535169, 598.60600	3	$199.5^{+99.8}_{-0}$	$0.6^{+0.17}_{-0.37}$	0	4.14	22.63
63	296737508	5.88 ± 0.36	20.97145, 733.99174	36	$23.7^{+6.9}_{-2.7}$	$0.6^{+0.12}_{-0.26}$	0	1.12	41.08
64	300394149	6.46 ± 0.34	19.69843, 748.53947	39	$26.0^{+16.0}_{-6.0}$	0.27 ± 0.22	0	4.92	36.29
65	303317324	2.67 ± 0.26	16.79925, 739.16710	45	$18.5^{+4.6}_{-1.7}$	0.12 ± 0.11	0	1.16	22.71
66	304339227	2.65 ± 0.17	27.48783, 714.68370	27	$31.1^{+8.6}_{-3.6}$	0.34 ± 0.24	0	2.19	13.81
67	306249066	11.09 ± 0.61	23.63027, 732.53786	32	$27.1^{+7.8}_{-3.5}$	0.867 ± 0.021	0	7.34	49.32
68	313671132	$7.78^{+0.67}_{-0.62}$	23.65724, 733.37241	32	$28.0^{+13.0}_{-5.0}$	$0.81^{+0.08}_{-0.22}$	0	7.02	27.41
69	317923092	$12.5^{+4.8}_{-1.4}$	19.19983, 729.59400	39	$27.0^{+19.0}_{-5.0}$	$0.928^{+0.062}_{-0.048}$	0	35.1	30.15
70	323295479	11.28 ± 0.6	67.50129, 742.51554	12	$83.0^{+41.0}_{-15.0}$	0.85 ± 0.013	0	2.43	138.65
71	332697924	4.69 ± 0.33	22.88951, 732.47218	33	$26.2^{+7.1}_{-3.3}$	0.34 ± 0.23	0	5.6	11.96
72	333736132	$10.25^{+0.87}_{-0.82}$	23.61270, 731.99390	32	$26.1^{+7.1}_{-2.5}$	$0.751^{+0.045}_{-0.091}$	0	13.92	55.96
73	339399841	$13.0^{+1.7}_{-1.1}$	22.44020, 381.48503	18	$25.4^{+9.2}_{-4.2}$	$0.73^{+0.15}_{-0.34}$	0	–	21.13
74	349091983	$21.3^{+8.8}_{-4.8}$	549.0649, 549.06501	1	549.0649	$0.975^{+0.075}_{-0.058}$	0	–	44.11
75	381553868	12.41 ± 0.84	20.91681, 690.25274	33	$23.8^{+6.2}_{-2.9}$	$0.39^{+0.22}_{-0.26}$	0	9.94	22
76	393229954	$9.3^{+4.1}_{-1.2}$	75.77521, 757.75214	11	$45.0^{+31.0}_{-0.0}$	$0.907^{+0.082}_{-0.098}$	0	12.97	33.63
77	394340183	10.87 ± 0.61	60.35608, 724.27290	10	$60.0^{+30.0}_{-18.0}$	0.29 ± 0.21	0	6.77	85.43
78	396720998	$1.45^{+0.96}_{-0.85}$	70.64108, 777.05180	12	$78.0^{+19.0}_{-13.0}$	0.46 ± 0.32	0	–	6.44
79	404518509	2.72 ± 0.17	23.45386, 703.61679	18	$23.0^{+12.0}_{-1.0}$	$0.35^{+0.28}_{-0.24}$	0	0.93	22.52
80	412386707	12.37 ± 0.81	23.33181, 746.61701	33	$25.7^{+6.7}_{-2.4}$	$0.65^{+0.15}_{-0.38}$	0	6.18	28.97
81	437293313	$8.57^{+0.56}_{-0.52}$	20.26060, 749.64177	38	27.0 ± 9.0	0.25 ± 0.2	0	–	26.34
82	439491923	13.9 ± 1.3	26.34748, 711.37923	28	$31.0^{+14.0}_{-5.0}$	$0.7^{+0.14}_{-0.3}$	0	–	36.2
83	442893494	$11.55^{+0.67}_{-0.63}$	21.87047, 721.72570	22	36.0 ± 12.0	$0.34^{+0.25}_{-0.23}$	0	–	24.76
84	457649900	$18.0^{+9.8}_{-3.9}$	23.40078, 748.82538	33	$30.0^{+20.0}_{-6.0}$	$0.986^{+0.058}_{-0.033}$	0	13.11	29.26
85	466206508	13.55 ± 0.82	25.04186, 375.62557	16	$31.0^{+16.0}_{-6.0}$	0.37 ± 0.2	0	12.81	64.68

Table A4. A sample of events from `monofind` that were not planetary in nature. This table is available in its entirety online.

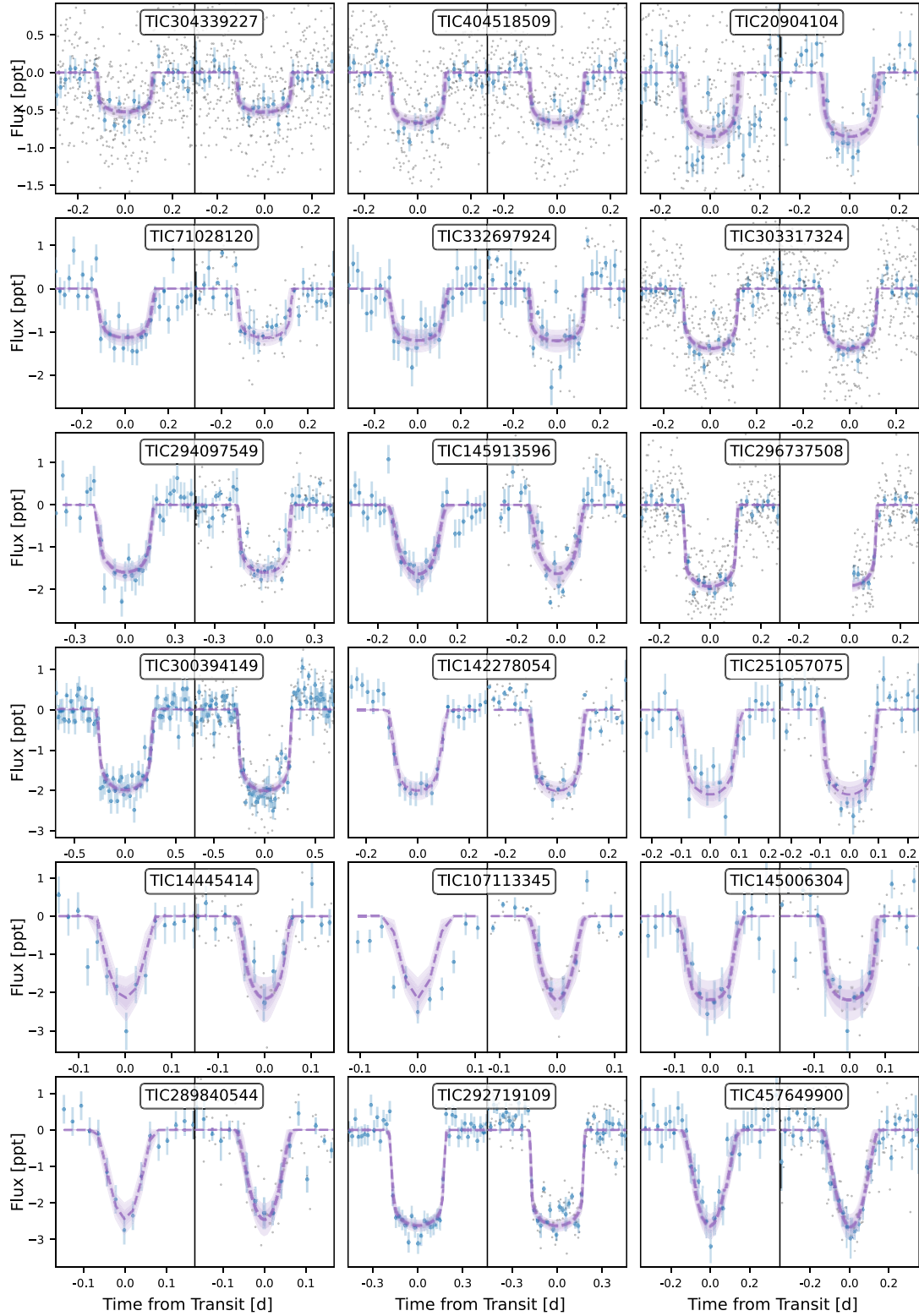| TIC ID	Designation	T_{c1}	T_{c2}
		(TBJD, [Sector])	(TBJD, [Sector])
82286	Asteroid	1606.56693 [11]	2337.34989 [38]
109979	Asteroid	1601.53746 [11]	2355.66990 [38]
2490309	Asteroid	1577.58862 [10]	2309.44366 [37]
3835932	Asteroid	1392.54454 [03]	2133.24553 [30]
5740937	Asteroid	1378.87982 [02]	2097.43075 [29]
–	–	–	–

Figure A1. Zoomed-in transit events for duotransit candidates TIC-304339227 to TIC-156716001 ordered by transit depth. The left panel shows the Year 1 transit, and the right panel shows the Year 3 transit. The data in blue are the *TESS* PDCSAP photometry (see Section 2). In cases with <15 min cadence blue points represent 30 min bins with raw photometry shown in grey. The dashed purple lines show the best-fitting transit model with 1 and 2 standard deviations as shaded purple regions.
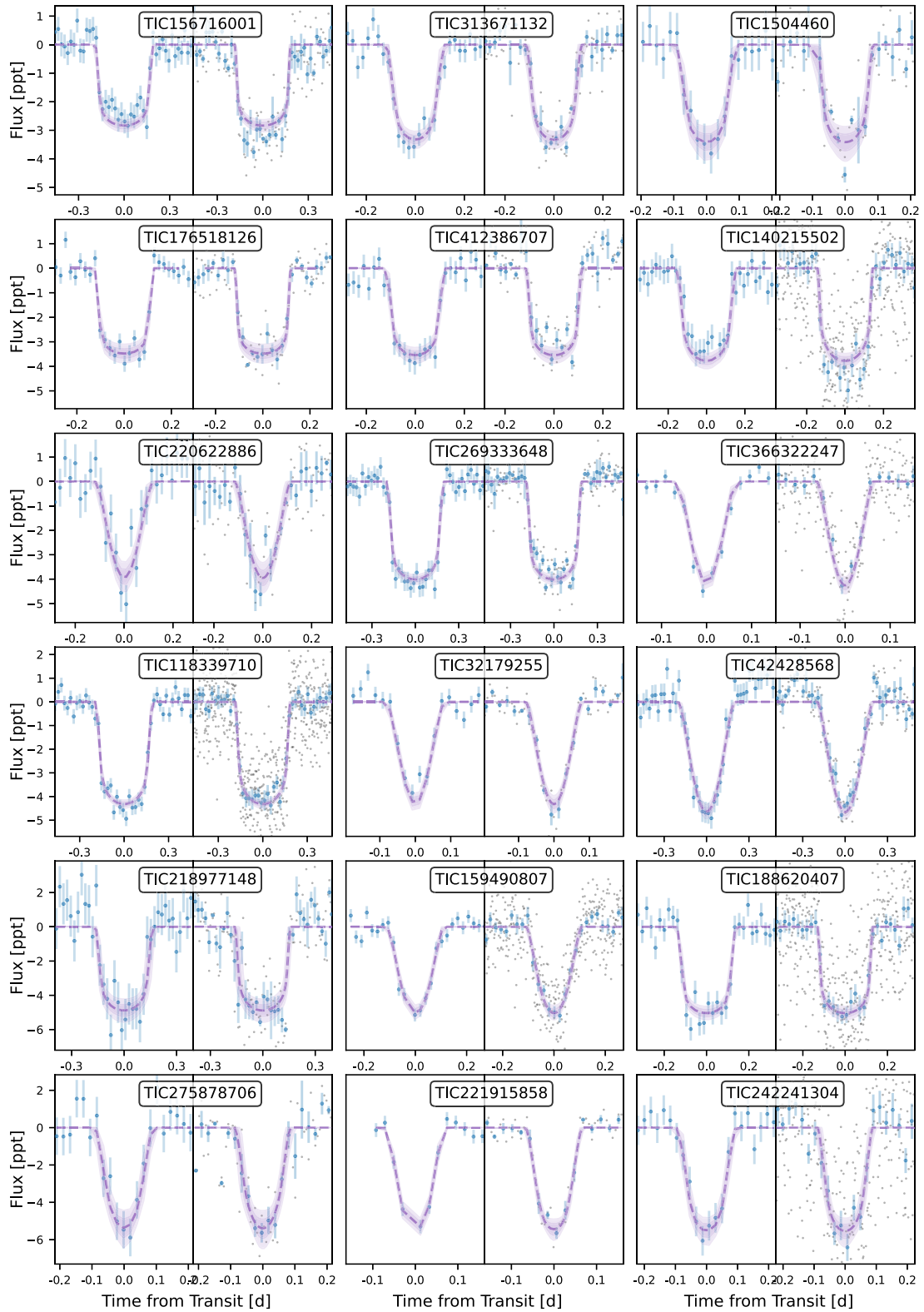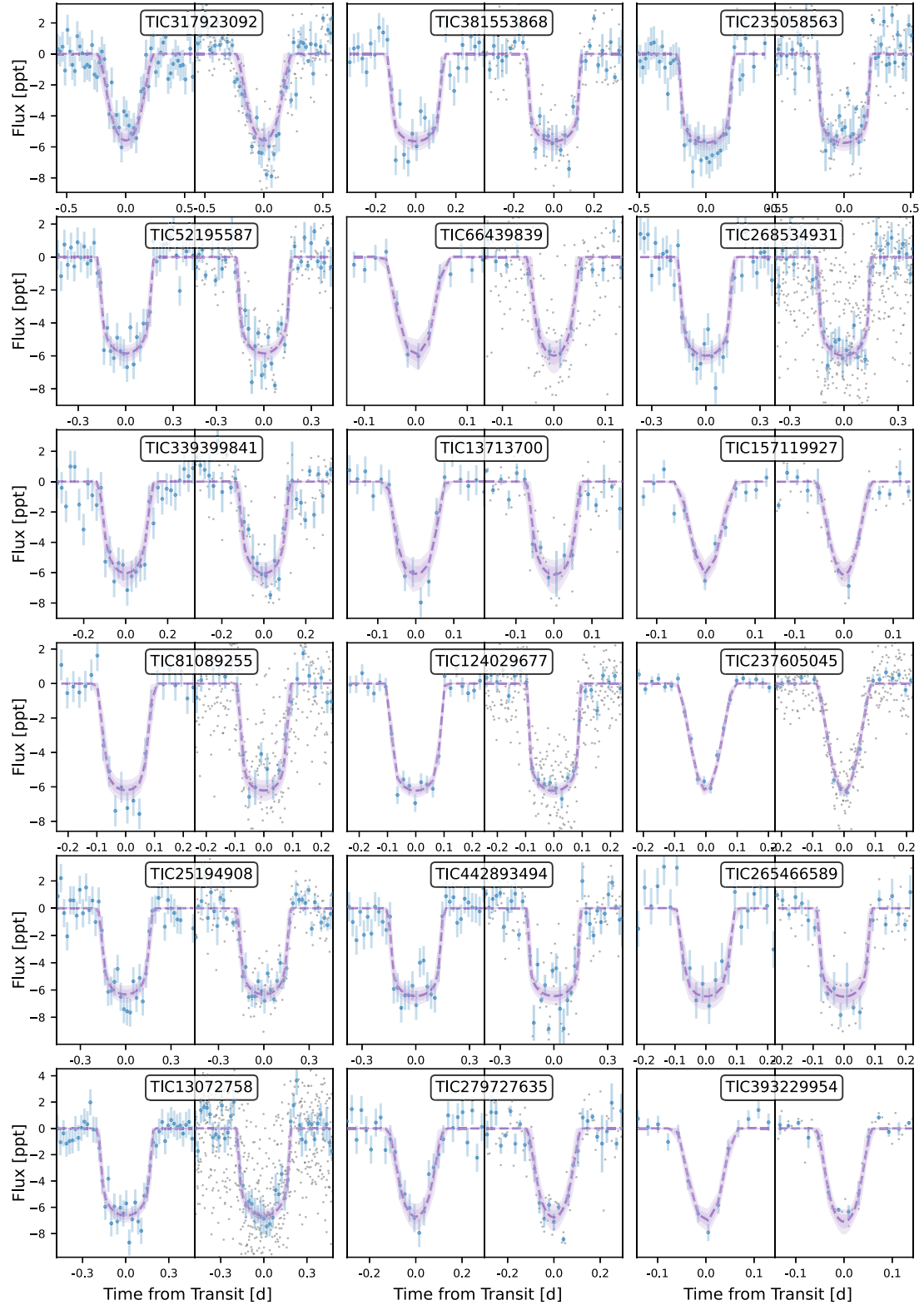
Figure A2. Zoomed-in transit events for duotransit candidates TIC-313671132 to TIC-381553868 ordered by transit depth. The left panel shows the Year 1 transit, and the right panel shows the Year 3 transit. The data in blue are the *TESS* PDCSAP photometry (see Section 2). In cases with <15 min cadence blue points represent 30 min bins with raw photometry shown in grey. The dashed purple lines show the best-fitting transit model with 1 and 2 standard deviations as shaded purple regions.

Figure A3. Zoomed-in transit events for duotransit candidates TIC-235058563 to TIC-306249066. The left panel shows the Year 1 transit, and the right panel shows the Year 3 transit. The data in blue are the *TESS* PDCSAP photometry (see Section 2). The dashed purple line is the best-fitting transit model with 1 and 2 standard deviations either side.
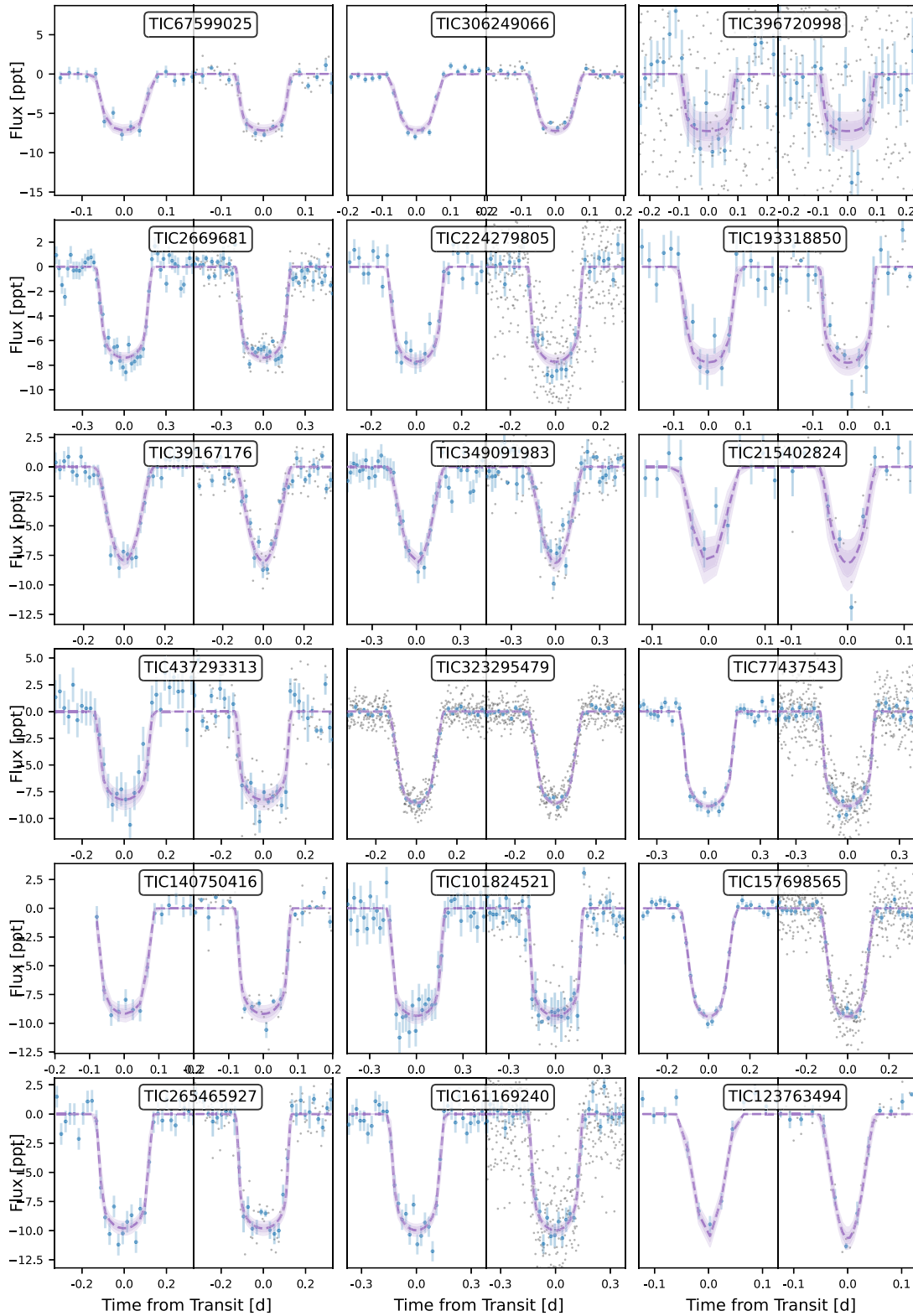
Figure A4. Zoomed-in transit events for duotransit candidates TIC-396720998 to TIC-439491923. The left panel shows the Year 1 transit, and the right panel shows the Year 3 transit. The data in blue are the *TESS* PDCSAP photometry (see Section 2). The dashed purple line is the best-fitting transit model with 1 and 2 standard deviations either side.
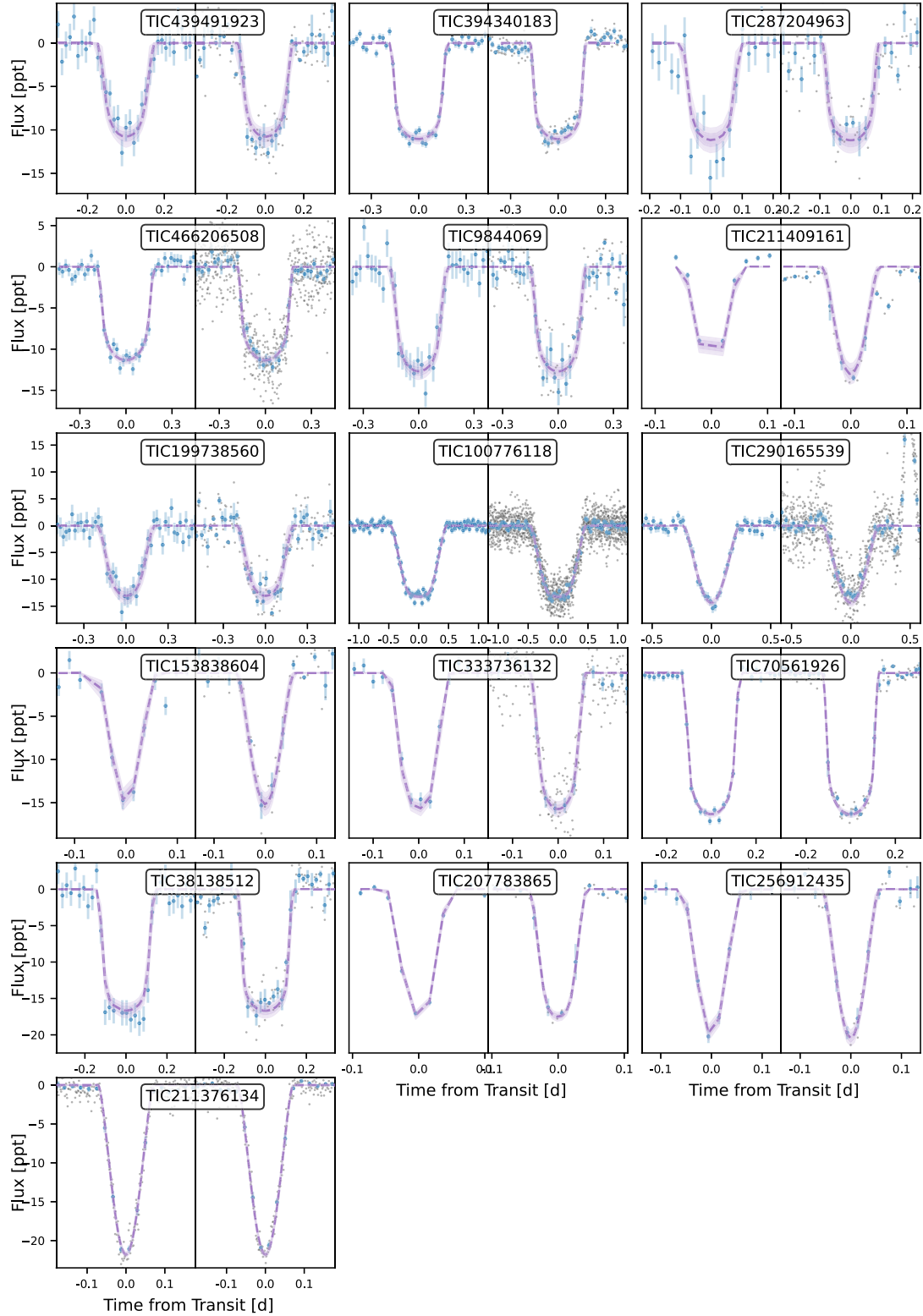
Figure A5. Zoomed-in transit events for duotransit candidates TIC-287204963 to TIC-256912435. The left panel shows the Year 1 transit, and the right panel shows the Year 3 transit. The data in blue are the *TESS* PDCSAP photometry (see Section 2). The dashed purple line is the best-fitting transit model with 1 and 2 standard deviations either side.

This paper has been typeset from a TEX/LATEX file prepared by the author.